C.P. No. 1293

C.P. No. 1293

PROCUREMENT EXECUTIVE, MINISTRY OF DEFENCE

AERONAUTICAL RESEARCH COUNCIL

CURRENT PAPERS

Low-Speed Wind-Tunnel Tests on the Lift-Dependent Drag of Delta Wings with Conical Camber

by

D. *L. I.* ***Kirkpatrick and P. J. Butterworth***

Aerodynamics Dept., R.A.E., Farnborough

LONDON: HER MAJESTY'S STATIONERY OFFICE

1974

PRICE 70p NET

UDC 533.6.013.127 : 533.693.3 : 533.6.043.1 : 533.6.044.5

* CP No.1293
June 1972

LOW-SPEED WIND-TUNNEL TESTS ON THE LIFT-DEPENDENT DRAG OF DELTA WINGS WITH CONICAL CAMBER

by

D. L. I. Kirkpatrick

P. J. Butter-worth

SUMMARY

This Report describes a theoretical method of designing cambered slender wings to have low lift-dependent drag. The results of subsonic wind-tunnel tests on a series of thin cambered delta wings of aspect ratio 2 are presented, and the significant drag reductions achieved are discussed in relation to theoretical predictions for the drag of cambered slender wings.

* Replaces RAE Technical Report 72123 - ARC 34085

CONTENTS

1 INTRODUCTION

The aerodynamics of a slender aerobus for short ranges has been reviewed in a recent paper [1], which considers an aircraft with a slender wing of near-delta planform, having an aspect ratio low enough to ensure flow separation at all its sharp edges, and with its engines installed above the wing sufficiently far from the edges to provide significant noise shielding. This paper shows that one of the most important problems in the design of such an aircraft is the relatively-high values of the lift-dependent drag factor K for thin slender wings. These high values of K arise because the flow separations at the leading edges of slender wings preclude the development of the high suction forces which generally occur at the leading edge of a wing in attached flow.

One method of solving this problem has been suggested by the results of recent wind-tunnel tests [2,3] which have shown that with increasing wing thickness the suction forces induced by the leading-edge vortices have an increasingly large forward component in the plane of the wing (so the lift-dependent drag of a thick slender wing is less than that of a thin wing of the same planform), and that the size of this forward component is controlled by the distribution of the wing thickness. These results suggest that the lift-dependent drag at take-off of a slender wing with a slenderness ratio of 0.5 and a thickness/chord ratio of 0.1 could be as much as 25% less than the lift-dependent drag of a thin slender wing with the same planform. However it may not be possible to use the optimum wing thickness distribution in a practical aircraft design.

Another method of reducing the lift-dependent drag is by cambering the wing so that the drag coefficient is a minimum when the lift coefficient is positive and the lift-dependent drag factor is a minimum at the critical flight condition, generally cruise or take-off. Some mild gothic wings designed using a linear theory [4] to give attached flow at specified values of the lift coefficient have been tested, and the results [5] show that the lift-dependent drag factor at take-off was reduced by up to 14%, albeit at the cost of increased incidence, depending on the degree of camber chosen.

A third distinct method of reducing the lift-dependent drag of a slender wing is by cambering it, not specifically to achieve minimum drag at positive lift, but to change the shape of the drag characteristic. Some preliminary calculations by Weber [6] suggested that the lift-dependent drag of a thin slender wing could be significantly reduced by cambering the wing so that the chordwise slope $\partial z/\partial x$ of its upper surface was large and positive in the regions where

the leading-edge vortices induced high suction forces, the forward components of which reduced the lift-dependent drag.

This Report describes some wind-tunnel tests on simple thin slender wings to find the drag reduction achieved by Weber-type camber, to assess the validity of a theoretical method of predicting this drag reduction, and to investigate whether the second and third methods quoted above can be used in combination to produce thin slender cambered wings with much lower values of lift-dependent drag than uncambered wings of the same planform.

2 THEORETICAL CALCULATIONS

Several years ago Weber[7] presented a method of calculating the shape of a slender wing so that at a specified value of the lift coefficient C_L the flow would not separate from the leading edge. This method is applicable to wings of any planform provided only that the apex is pointed, the trailing edge is unswept and the chordwise rate of change of semispan is nowhere negative ($\partial s/\partial x \geqslant 0$). The shape $z(x,y)$ of the wing camber surface is determined as that of a stream surface by applying the linearised boundary condition that

$$\frac{\partial z(x,y)}{\partial x} = \frac{v_z(x,y,0)}{V_\infty} ,$$

where V_∞ is the velocity of the undisturbed flow and v_z is the velocity component in the cross-flow plane. The spanwise distributions of the downwash v_z are specified[7] in terms of $\eta = y/s(x)$ and the distributions considered are such that at a chordwise station x = constant, the downwash is constant over the inner part of the wing $0 < |\eta| < \eta_0(x)$ and over the outer part of the wing $\eta_0(x) < |\eta| < 1$ the downwash is given by a constant or by a linear or quadratic function of η, *viz* -

$$\frac{v_z(x,y,0)}{V_\infty} = \begin{cases} C(x) & \text{for } 0 < |\eta| < \eta_0 \\ C(x) + D_\nu(x)\left[\frac{|\eta| - \eta_0(x)}{1 - \eta_0(x)}\right]^{\nu-1} & \text{for } \eta_0 < |\eta| < 1 \end{cases}$$

where ν = 1, 2 or 3. The relationship between $D_\nu(x)$ and $C(x)$, in terms of $\eta_0(x)$, is specified by the condition of zero loading at the leading edge in attached flow. From the chosen expression for the local slope $\partial z(x,y)/\partial x = v_z/V_\infty$, the shape of a chordwise section $z(x, y = \text{const.})$ can be

determined by integration except for an arbitary additive term f(y) (for example f(y) can be chosen to make the trailing edge straight, i.e. $z(1,y)$ = constant). The aerodynamic loading on the chosen wing in attached flow, and hence the lift, drag and pitching moment on it, can be calculated from the downwash/local slope distribution using slender-wing theory.

If the local aerodynamic loading on an uncambered slender wing at incidence α is $\ell(x,y) = -\Delta C_p(x,y)$, then its lift-dependent drag is

$$C_{D_i} = \frac{1}{S}\int_0^c \int_{-s(x)}^{s(x)} \alpha \ell(x,y)\,dy\,dx = \alpha C_L ,$$

where c is the wing chord, $s(x)$ the semispan and S the plan area. In this Report, the incidence α of a slender wing at any chosen attitude is defined as the angle between the wing chord at that attitude and the wing chord when the flow does not separate at the leading edge. For the special case of uncambered wings, α is the angle between the wing chord and the free stream. The induced drag of a slender wing of the same planform but cambered so that its surface slope is $\left(\alpha - \frac{\partial z(x,y)}{\partial x}\right)$ is therefore

$$C_{D_i} = \frac{1}{S}\int_0^c \int_{-s(x)}^{s(x)} [\ell(x,y) + \Delta\ell(x,y)]\left[\alpha - \frac{\partial z(x,y)}{\partial x}\right] dy\,dx ,$$

where $\Delta\ell(x,y)$ is the loading increment induced by the camber. If the flow is conical so that the spanwise position of the leading-edge vortices is independent of x (i.e. η_v = const.) and if the chosen camber is such that C and η_0 are also independent of x, then

$$C_{D_i} = \int_0^1 [\ell(\eta) + \Delta\ell(\eta)]\left[\alpha - \frac{\partial z(\eta)}{\partial x}\right] d\eta$$

$$= \alpha[C_L + AC_L] - \int_0^1 \ell(\eta)\,\frac{\partial z(\eta)}{\partial x}\,d\eta - \int_0^1 \Delta\ell(\eta)\,\frac{\partial z(\eta)}{\partial x}\,d\eta ,$$

where AC_L is the camber-induced increment of lift on the wing. Because the loading $\ell(\eta)$ has its largest values on the part of the wing below the leading-edge

vortices, the second term in the above expression is negative if the camber is chosen so that $\partial z(\eta)/\partial x$ is large and positive at $\eta = \eta_v$. The third term is generally relatively small because both $\Delta\ell(\eta)$ and $\partial z(\eta)/\partial x$ are small for the camber distributions which yield practical wing shapes. The lift-dependent drag factors of the plane and cambered wings at the same incidence are given by the expressions

$$\frac{K(\text{plane})}{\pi A} = \frac{\alpha}{C_L}$$

and

$$\frac{K(\text{cambered})}{\pi A} = \frac{\alpha}{C_L + \Delta C_L} - \frac{1}{(C_L + \Delta C_L)^2} \int_0^1 \frac{\partial z(\eta)}{\partial x} [\ell(\eta) + \Delta\ell(\eta)] d\eta$$

Thus low values of K(cambered) can be achieved by designing the wing either to make ΔC_L large or to make the integral in the second term large and positive.

The lift-dependent drag reduction which can be achieved by camber may be calculated if it is assumed that

(1) the spanwise distribution of aerodynamic loading on a plane slender wing is similar to that predicted by Kiichemann's non-linear lifting-surface theory[8], viz.,

$$\ell(\eta) = \frac{C_L(x)}{\pi} \frac{1}{\sqrt{1 - \eta_v^2}} \log \frac{\sqrt{1 - \eta_v^2} + \sqrt{1 - \eta^2}}{\left|\sqrt{1 - \eta_v^2} - \sqrt{1 - \eta^2}\right|} ,$$

where $C_l(x) = \int_0^1 \ell(\eta) d\eta$ is the local loading coefficient

and $C_L(x) = C_L$ in conical flow, and

(2) the development of the leading-edge vortices above the wing, i.e. the variation with incidence of η_v and $C_l(x)$ is not significantly affected by the small amounts of camber considered in this Report.

Fig.1 compares the loading distribution predicted by Küchemann[8] for two chosen values of η_v with experimental loading distributions measured on a thin uncambered delta wing, and suggests that Kiichemann's expression for $\ell(\eta)$ is

sufficiently accurate for preliminary calculations. The effect of camber on the spanwise positions of the leading-edge vortices cannot accurately be predicted, though some experimental results[5,10] suggest that the vortices move outboard with increasing camber, so it is reasonable to hope that the slight movement of the vortices, induced by the small camber of the wings tested, will not significantly affect the loading distribution or lead to serious errors, This hope is strengthened by Fig.2 which presents the results measured by Kirby and Cox[11] on conical slender wings with drooped leading edges and shows that the variation with incidence of the vortex-induced lift is unaffected by camber. This implies that

$$C_L(\text{cambered}) = C_L(\text{plane}) + \Delta C_L ,$$

where the camber-induced lift increment, ΔC_L, is independent of incidence.

The lift-dependent drag of a cambered delta wing at a particular value of $\alpha/\cot\phi$, where ϕ is the sweepback angle of the leading edge, may therefore be calculated by finding η_v from correlated experimental results[12], using Kiichemann's theory[8] to predict $\ell(\eta)$ and CL, using Weber's theory[7] to predict $\Delta\ell(\eta)$ and ΔC_L, and calculating K(cambered) from the equation above. Alternatively, if experimental results have been obtained for an uncambered wing of the appropriate planform, K(cambered) may be calculated using an empirical value of C_L and a $\ell(\eta)$ distribution obtained from experimental results, such as those plotted in Fig.1. This latter method of calculation should yield more accurate results, particularly if the wing considered is not very slender. The calculations for the wings tested in this experiment are presented in detail in the Appendix.

3 DESCRIPTION OF WINGS TESTED AND EXPERIMENTAL PROCEDURE

The wings tested in this experiment were designed to investigate the validity of the method (described in section 2) of predicting reductions in the lift-dependent drag. No attempt was made to select optimum camber distributions to obtain the minimum lift-dependent drag. For simplicity of calculation and ease of manufacture, conical cambered delta wings were used, and the results are compared with those of an uncambered delta wing of the same aspect ratio (A = 2.0). The shapes of the four cambered wings (see Fig.3) were calculated using $\nu = 1$ or $\nu = 2$ downwash distributions as presented in the table below and discussed in the following paragraphs.

Wing	Discontinuity η_0 =	Downwash distribution type, ν =	C(x)	ΔC_L	α_c, deg (at $\alpha = 0$)
Double-kinked	0.6 0.9	1 1	0.1 -0.0595	0	2.45
Kinked	0.6	1	0.1	0.163	5.73
Kinked	0.6	1	0.05	0.0815	2.87
Curved	0.5 0.8	2 2	0.123 -0.0316	0.163	5.24

The first of the cambered wings was designed to discover whether Weber's forecast was correct and a significant reduction in lift-dependent drag can be achieved by cambering a slender wing while keeping the camber-induced lift increment ΔC_L equal to zero. The shape of this wing (see Fig.3) was calculated by superimposing two $\nu = 1$ downwash distributions with discontinuities at $|\eta| = 0.6$ and 0.9. These distributions were chosen so that $\partial z(\eta)/\partial x$ would be positive when $0.6 < |\eta| < 0.9$ because experimental results[12] suggest that the leading-edge vortices would be above these parts of the wing in the incidence range given by $0.1 < cl/\cot \phi < 1.0$ which includes the take-off incidence of slender aircraft. The ratio of the values of C for the two downwash distributions was chosen so that the camber-induced lift increment AC_L equals zero at the attachment incidence, and the magnitude of the values was chosen in the hope that they would be large enough to yield significant reductions in lift-dependent drag but small enough to avoid undesirable flow separations from the discontinuity lines at $|\eta| = 0.6$ and 0.9.

From the beginning of this investigation, it was realised that the first camber shape would be unfavourable in cruise, when the leading-edge vortices would lie close to the leading edges so that $\partial z(\eta)/\partial x$ would be negative below the vortices, and that further reductions in lift-dependent drag might be achieved by changing the camber so that ΔC_L became positive. A second wing was therefore designed by removing the discontinuity at $|\eta| = 0.9$ so that $\partial z(\eta)/\partial x$ was constant and positive in the range $0.6 < |\eta| < 1.0$.

The results for the first two cambered wings were expected to suggest that it would be useful to have a leading-edge flap set at different angles to optimise the aircraft configuration for cruise, take-off and approach conditions; the spanwise distribution of f(y), which determines the wing shape (see

section 2), for the first two wings was therefore determined by the requirement that the (hinge) lines at $|\eta| = 0.9$ should be straight. If Weber's theory[7] is correct (see section 2), similar results would be obtained from wings with different spanwise distributions of f(y), e.g. with straight trailing edges.

To investigate how the wing performance varied with the amount of camber, a third cambered wing was made with exactly half the camber of the second wing. These two wings can thus be regarded as members of the same family of cambered wings.

It was hoped that removing the sharp kinks at $|\eta| = 0.6$ in the downwash distribution of the second cambered wing would appreciably reduce the value of the minimum drag coefficient, so a fourth cambered wing was designed using two $v = 2$ downwash distributions. The ratio of the values of C for these distributions was chosen so that $\partial z(\eta)/\partial x$ was constant and positive when $|\eta| > 0.8$ and the magnitude of the values of C was chosen to give the same value of $\Delta C_L = 0.163$ as the second wing. For the fourth wing the function f(y) was chosen so that the leading edge was a straight line.

Fig.3 shows each of the wings, at zero incidence, viewed from downstream along the free-stream velocity vector. This figure also compares the values of the wetted area S_W and the frontal area Φ for each of the four cambered wings with the values for the uncambered wing. The quoted values of the camber-induced lift ΔC_L at zero incidence were calculated using Weber's theory[7]. Each of the wings was made from 16-gauge steel plate with the leading and trailing edges chamfered symmetrically. On the kinked and double-kinked wings, the shoulders at $|\eta| = 0.6$ and $|\eta| = 0.9$ were faired with radii of curvature of about 6 mm (0.25 inch).

The wings were hung on the standard wire rig in the 4ft × 3ft low-speed wind tunnel, and surface flow visualization tests were made at a wind speed of 24.4 m/s (80 ft/s) to find whether the swept discontinuity lines on the kinked or double-kinked wings caused the flow to separate and form vortices. The flow visualization tests were made at 5 degree intervals throughout the incidence range, and showed that at some positive incidences there was evidence of small separation bubbles in the lee of the shoulders but that at no incidence aid these separations induce strong vortices. The lift, drag and pitching moment on each wing were then measured on the wind-tunnel balance over the incidence range $-4 < \alpha < 25$ degrees at a wind speed of 24.4 m/s, corresponding to a Reynolds number based on centreline chord of 0.64 million. This comparatively-low wind

speed was dictated by the need to avoid significant distortion of the wings, which had an unusually small thickness/chord ratio of 0.004. However, because the wings had sharp edges, scale effects should have been negligibly small [13].

4 DISCUSSION OF RESULTS

The measured values of the lift, drag and pitching moment coefficients for the uncambered and cambered wings were corrected for wind-tunnel constraint and the effects of the wire rig, and were plotted in Figs.4-7.

Fig.4 presents the variation of the lift coefficient with the angle of incidence α (which differs from the centre-line incidence α_c as shown on Fig.4) and shows that the point of inflexion of each of the measured lift characteristics, i.e. the point at which there is no flow separation at the leading edges, is close to the theoretical attachment incidence $\alpha = 0$. At this incidence the measured values of the lift coefficient are slightly smaller (see table on Fig.4a) than the calculated values of the camber-induced lift ΔC_L, because of the need to satisfy the Kutta condition at the trailing edge in subsonic flow. This figure also shows that the shape of the lift characteristics of all the cambered wings are very similar, unless α is quite large, and thus supports the earlier assumption that the vortex development is not significantly affected by small amounts of camber.

Fig.5 presents the measured lift coefficients plotted against the centre-line incidence α_c. It is shown that

(1) at any given centre-line incidence the results for the three kinked wings (including the basic plane wing) of the same family demonstrate that the lift coefficient varies continuously with the degree of camber,

(2) the lift characteristics of the kinked and curved cambered wings with the same value of $\Delta C_L = 0.163$ are not significantly different, and

(3) at any given centre-line incidence the lift of the double-kinked wing ($\Delta C_L = 0$) is only slightly greater than that of the kinked wing ($\Delta C_L = 0.163$). This suggests that the angle $\partial z/\partial x$ of the outermost 10% of the wing semispan does not have an important effect on the lift characteristic of the wing.

Fig.6 shows that all the cambered wings have larger values of the minimum drag coefficient than the uncambered wing, but that at moderate and high lift coefficients the drag of the cambered wings is considerably lower than that of

the uncambered wing. To illustrate the size of this drag reduction, the drag coefficients measured for the various wings at CL = 0.5, (a typical take-off lift coefficient for a slender-wing aircraft) are tabulated below:-

Wing	ΔC_L	Min. C_D	$C_D(C_L = 0.5)$	Drag reduction at $C_L = 0.5$
Uncambered	0	0.0098	0.1054	
Double-kinked	0	0.0136	0.0910	14%
Kinked	0.163	0.0155	0.0815	23%
Kinked	0.0815	0.0105	0.0951	10%
Curved	0.163	0.0152	0.0896	15%

Fig.7 shows that the shapes of the pitching moment characteristics of all the wings are similar, but that the kinked and double-kinked cambered wings experienced pitch-up at lower values of lift than the uncambered wing. All the cambered wings sustained appreciable pitching moments at zero lift and these moments, as well as the shapes of the pitching moment characteristics, had a significant effect on the loss of lift due to trimming. To illustrate this effect, the untrimmed and trimmed values of C_L at an arbitrarily-chosen value of the centre-line incidence are given in the following table, assuming that each wing is trimmed for neutral stability at that incidence and balanced using a trailing-edge flap whose point of action is at a typical position at 0.85 c from the apex.

Wing	ΔC_L	α_c, deg	C_L (untrimmed)	C_L (trimmed)	Trim loss
Uncambered	0	14	0.648	0.623	4%
Double-kinked	0	14	0.484	0.415	15%
Kinked	0.163	14	0.465	0.442	5%
Kinked	0.0815	14	0.542	0.521	4%
Curved	0.163	14	0.466	0.438	6%

These figures for the percentage loss of lift due to trimming for the uncambered, curved and two kinked wings imply that the drag increments due to trimming for these wings are similar in size, so the reductions in trimmed drag for these wings are likely to be very close to the untrimmed drag reductions

quoted above. The double-kinked wing has a larger loss of lift due to trimming and consequently a larger drag increment than the other wings, so the trimmed drag reduction for this wing might be considerably less than the value of 14% reduction in untrimmed drag quoted above.

The shape of the pitching moment characteristics of the cambered slender wings is likely to be significantly affected by the assumed value of the arbitrary term f(y) which determines the shape of the wing trailing edge (see section 2), by the wing thickness and thickness distribution, and by the position of the fuselage and nacelles. The lift loss due to trimming is also affected by the control characteristics. Consequently the quoted values of trim lift loss should be regarded only as indicative of the loss on a real aircraft with a cambered slender wing.

5 ANALYSIS OF RESULTS

In a discussion of the drag characteristics of cambered wings, Warren[14] assumes that the lift-dependent drag is governed by a factor K', which is dependent on the wing planform and camber shape but is independent of the amount of camber, so that

$$C_D = C_{D_m} + K'(C_L - C_{L_m})^2/\pi A \ ,$$

where C_{D_m} is the minimum drag coefficient of a cambered wing and C_{L_m} is the lift coefficient at which the minimum drag coefficient occurs. This equation implies that the drag polars of a family of cambered wings have the same shape but have their minima at different values of (C_{L_m}, C_{D_m}). Fig.8 presents the variation of K' for the cambered wings tested in this experiment and the lowest part of this figure, which includes three wings with different amounts of the same type of camber, shows that K' is affected by the amount of camber so that it is not possible to use the results from one cambered wing directly to estimate the drag characteristics of another wing with a different amount of camber.

To demonstrate the reduction of wing drag due to camber, Fig.9 presents the variation with lift of the lift-dependent drag factor $K = \pi A(C_D - C_{D_0})/C_L^2$ where C_{D_0} is the profile drag of the plane wing, and shows that at a chosen lift coefficient the values of the lift-dependent drag on the cambered wings are significantly less than that on the plane wing. At a typical take-off lift coefficient of 0.5 the largest measured reduction in K is 26% (for the kinked wing $\Delta C_L = 0.163$).

Fig.10 shows the variation with incidence of the measured values of $K = \pi A(C_D - C_{D_0})/C_L^2$ for the plane and cambered wings, and compares the differences with the results of theoretical calculations (see Appendix). The measured values of K for the two wings with ACL = 0 increase as the incidence tends to zero, because of the non-linearity of the lift characteristics and became CD, $> C_{D_0}$ for the double-kinked wing. However the measured values of K for the other wings tested decrease as incidence tends to zero. Fig.10 also shows that the calculations (see section 2) using empirical values of CL and $\ell(\eta)$ [9] predict the camber-induced reduction in lift-dependent drag more accurately than calculations using theoretical values of CL and $\ell(\eta)$. This suggests that the former type of calculation should be used, if sufficient experimental data is available, to design improved camber distributions and predict their performance. 14

6 CONCLUDING REMARKS

The results of the experiments presented in this Report have demonstrated that significant reductions in the lift-dependent drag of a slender wing can be achieved by the use of camber, and that the extent of this reduction can be predicted with reasonable accuracy using the methods described above.

Camberedwings of the type tested may be especially suitable for a quiet slender aerobus because, if the engines were mounted above such a wing near the centre-line and if the outer parts of the wing were designed to be significantly higher than the centre-line, the lateral noise from the engines during the take-off ground run would be deflected away from the ground.

The amount of camber, and hence the extent of the lift-dependent drag reduction, will probably be limited by the onset of flow separation from the wing upper surface or by the need to avoid excessive camber-induced profile drag at cruising speed. The onset of upper-surface flow separations, as well as the size of camber-induced effects on performance, may well be significantly influenced by the wing thickness distribution. Consequently the optimum camber shape and the optimum degree of camber for a particular slender aircraft with specified range, payload and performance can only be determined from project studies and associated wind-tunnel tests on real aircraft configurations.

Appendix

CALCULATION OF REDUCTIONS IN INDUCED DRAG

The conically-cambered wings tested in these experiments were cambered using the $\nu = 1$ and $\nu = 2$ downwash distributions given by Weber's[7] equations (7) and (8) as:

$$\nu = 1 : \quad \frac{v}{V_\infty} - \frac{z}{V} = C \qquad 0 < |\eta| < \eta_0$$

$$= C\left(1 - \frac{\pi/2}{\cos^{-1}\eta_0}\right) \qquad \eta_0 < |\eta| < 1$$

$$\nu = 2 : \quad -\frac{v_z}{V_\infty} = C \qquad 0 < |\eta| < \eta_0$$

$$= C\left(1 - \frac{\pi(|\eta| - \eta_0)}{2\left(\sqrt{1 - \eta_0^2} - \eta_0 \cos^{-1}\eta_0\right)}\right) \qquad \eta_0 < |\eta| < 1$$

where η_0 is the spanwise position of the downwash discontinuity. The combinations of downwash distributions used, their points of discontinuity (η_0) and the values of C used in the design of the four cambered wings tested are given in the table in section 3. According to Weber's[7] equations (50) and (51), the lift increment induced by the camber for the $\nu = 1$ and $\nu = 2$ distributions is given by

$$\nu = 1 : \quad \Delta C_L = 2\pi C \cot \frac{\eta_0\sqrt{1 - \eta_0^2}}{\cos^{-1}\eta_0}$$

$$\nu = 2 : \quad \Delta C_L = 2\pi C \cot \phi \frac{(1 - \eta_0^2)^{3/2}}{3\left(\sqrt{1 - \eta_0^2} - \eta_0 \cos^{-1}\eta_0\right)}$$

It is shown in section 2 that the values of the induced drag on plane and conically-cambered wings at the same incidence α are given by the expressions:

$$C_{D_i}(\text{plane}) = \alpha C_L$$

$$C_{D_i}(\text{cambered}) = \alpha(C_L + \Delta C_L) - C_L \int_0^1 \frac{\ell(\eta)}{C_L} \frac{\partial z(\eta)}{\partial x} d\eta - \int_0^1 \Delta\ell(\eta) \frac{\partial z(\eta)}{\partial x} d\eta \quad .$$

Because the value of R(n) predicted by Küchemann[8] tends to infinity below the leading-edge vortices, (i.e. when $\eta = \eta_v$) it is convenient to rewrite the integral including $\ell(\eta)$ in the form:

$$\int_0^1 \frac{\ell(\eta)}{C_L} \frac{\partial z(\eta)}{\partial x} d\eta = \frac{\partial z(\eta_v)}{\partial x} + \int_0^1 \frac{\ell(\eta)}{C_L} \left[\frac{\partial z(\eta)}{\partial x} - \frac{\partial z(\eta_v)}{\partial x} \right] d\eta \quad ,$$

since the integrand on the right-hand side of this equation is zero when $\eta = \eta_v$. In this way, $\int_0^1 \frac{\ell(\eta)}{C_L} \frac{\partial z(\eta)}{\partial x} d\eta$ may be evaluated using either Küchemann's[8] loading distributions or the empirical distributions plotted in Fig.1 (though in this latter case the integral can be evaluated directly).

According to Weber's[7] equations (32) and (33) for conically-cambered wings, the camber-induced loading distributions for v = 1 and v = 2 downwash distributions are given by:

$$v = 1: \quad \Delta\ell(\eta) = 2c \cot\phi \frac{\eta_0}{\cos^{-1}\eta_0} \ln \frac{\sqrt{1-\eta^2} + \sqrt{1-\eta_0^2}}{\left|\sqrt{1-\eta^2} - \sqrt{1-\eta_0^2}\right|}$$

$$v = 2: \quad \Delta\ell(\eta) = C \cot\phi \frac{1}{\sqrt{1-\eta_0^2} - \eta_0 \cos^{-1}\eta_0} \left\{ 2\sqrt{1-\eta_0^2}\sqrt{1-\eta^2} + (\eta_0^2-\eta^2) \ln \frac{\left|\sqrt{1-\eta^2} - \sqrt{1-\eta_0^2}\right|}{\sqrt{1-\eta^2} + \sqrt{1-\eta_0^2}} \right\} .$$

The values of $\Delta\ell(\eta)$ and $\Delta\ell(\eta) \frac{\partial z(\eta)}{\partial x}$ for the three types of cambered wings were calculated and are plotted against η in Fig.11. The tables below show some of the steps in the calculations of $\frac{K(\text{cambered})}{K(\text{plane})}$.

Wing	α^{o}_{DES}	$C_{L_{DES}}$	$\alpha/\alpha/\cot\phi\phi$	η_v	$F(\eta_v)$	C_L	ΔC_L	$\int_0^1 \frac{\ell(\eta)}{C_L}\frac{\partial z}{\partial x}\,d\eta$	$\int_0^1 \frac{\Delta\ell(\eta)}{\alpha C_L}\frac{\partial z}{\partial x}\,d\eta$	$\frac{C_{D_i}\text{ (cam)}}{C_{D_i}\text{ (plane)}}$	$\frac{C_L\text{ (cam)}}{C_L}$	$\frac{K\text{(cam)}}{K\text{(plane)}}$
Calculations using Küchemann's prediction of $\ell(\eta)$ and C_L:												
Kinked	5.73	0.163	0.25	0.8	1.457	0.572	0.163	-0.107	-0.088	1.478	1.283	0.900
			0.50	0.7	1.542	1.211	0.163	-0.095	-0.020	1.249	1.134	0.971
Curved	5.24	0.163	0.25	0.8	1.457	0.572	0.163	-0.126	-0.084	1.495	1.283	0.908
			0.50	0.7	1.542	1.211	0.163	-0.123	-0.020	1.277	1.134	0.993
Double kinked	2.45	0.0	0.25	0.8	1.457	0.572	0	0.270	-0.026	0.756		0.756
			0.50	0.7	1.542	1.211	0	0.110	-0.006	0.896		0.896
Calculations using empirical values of $\ell(\eta)$ and C_L:												
Kinked	5.73	0.163	0.25	0.8		0.31	0.163	0.073	-0.161	1.610	1.522	0.695
			0.50	0.7		0.664	0.163	-0.014	-0.038	1.297	1.245	0.837
Curved	5.24	0.163	0.25	0.8		0.31	0.163	0.193	-0.155	1.484	1.522	0.641
			0.50	0.7		0.664	0.163	-0.054	-0.036	1.335	1.245	0.861
Double kinked	2.45	0.0	0.25	0.8		0.31	0	0.275	-0.046	0.771		0.771
			0.50	0.7		0.664	0	0.134	-0.011	0.877		0.877

Table 1

UNCAMBERED WING

α_c	C_L	C_D	C_m	K
-3.74	-0.1432	0.01890	0.00731	
-2.71	-0.1095	0.01572	0.00444	
-1.61	-0.0647	0.01172	0.00308	
-1.15	-0.0497	0.01000	0.00269	
-0.72	-0.0259	0.01149	0.00106	
-0.21	-0.0079	0.01131	0.00065	
0.26	0.0096	0.00980	-0.00033	
0.73	0.0281	0.01031	-0.00239	
1.29	0.0456	0.01034	-0.00111	
1.72	0.0702	0.01173	-0.00210	
2.19	0.0889	0.01296	-0.00395	
3.17	0.1288	0.01648	-0.00305	
4.16	0.1659	0.02139	-0.00425	2.646
5.15	0.2110	0.02842	-0.00458	2.628
6.20	0.2551	0.03618	-0.00490	2.547
7.09	0.3017	0.04724	-0.00565	2.584
8.03	0.3474	0.05737	-0.00573	2.476
9.13	0.3891	0.07102	-0.00587	2.541
10.08	0.4460	0.08666	-0.00673	2.428
11.03	0.4975	0.10434	-0.00700	2.400
12.02	0.5436	0.12369	-0.00793	2.422
13.08	0.5962	0.14646	-0.00758	2.416
14.02	0.6470	0.16911	-0.00783	2.391
14.97	0.6963	0.19384	-0.00666	2.385
16.02	0.7454	0.21982	-0.00464	2.375
17.06	0.7872	0.24654	-0.00270	2.401
18.06	0.8329	0.27748	-0.00219	2.424
19.00	0.8823	0.30876	-0.00285	2.413
19.92	0.9032	0.33470	0.00135	2.502
20.97	0.9452	0.36857	0.00043	2.523

Table 2

DOUBLE-KINKED WING: AC, = 0

α_c	C_L	C_D	C_m	K	K'
-1.75	-0.1783	0.03335	0.00437		
-0.82	-0.1437	0.02490	-0.00008		
0.08	-0.0911	0.01863	0.00382		
0.50	-0.0743	0.01706	-0.00305		
1.07	-0.0490	0.01583	-0.00293		
1.59	-0.0263	0.01513	-0.00406		
2.11	-0.0096	0.01394	-0.00469		
2.59	0.0163	0.01411	-0.00530		
3.05	0.0322	0.01379	-0.00652		
3.62	0.0541	0.01416	-0.00710		
4.03	0.0664	0.01469	-0.00729		
4.71	0.0913	0.01577	-0.00765		
5.02	0.1083	0.01583	-0.00780		
5.54	0.1280	0.01775	-0.00869		
6.49	0.1715	0.02068	-0.01032		
7.47	0.2078	0.02664	-0.00981		
8.46	0.2526	0.03188	-0.01110	2.174	2.277
9.40	0.2928	0.03848	-0.01157	2.102	2.229
10.39	0.3283	0.04611	-0.01102	2.117	2.265
11.38	0.3728	0.05574	-0.01146	2.077	2.227
12.42	0.4169	0.06610	-0.01104	2.035	2.181
13.36	0.4584	0.07784	-0.01106	2.034	2.179
14.40	0.4971	0.08993	-0.00941	2.037	2.179
15.34	0.5389	0.10600	-0.00903	2.081	2.224
16.33	0.5791	0.12244	-0.00801	2.110	2.252
17.32	0.6233	0.14206	-0.00801	2.139	2.278
18.31	0.6659	0.16187	-0.00697	2.155	2.289
19.21	0.7124	0.18572	-0.00717	2.178	2.309
20.15	0.7566	0.21160	-0.00718	2.215	2.344
21.14	0.7985	0.23851	-0.00637	2.254	2.380
22.19	0.8427	0.27128	-0.00579	2.314	2.439
23.13	0.8902	0.30606	-0.00620	2.349	2.472

Table 3

KINKED WING: $\Delta C_L = 0.163$

α_c	C_L	C_D	C_m	K	K'
-1.83	-0.2024	0.04530	0.00775		
-0.78	-0.1547	0.03558	0.00653		
0.21	-0.1135	0.02933	0.00675		
1.11	-0.0662	0.02245	0.00427		
2.05	-0.0207	0.01935	0.00310		
3.09	0.0187	0.01615	0.00193		
4.13	0.0627	0.01503	0.00057		
5.06	0.0977	0.01496	-0.00060		
5.58	0.1172	0.01672	-0.00125		
6.11	0.1403	0.01682	-0.00190		
6.57	0.1534	0.01739	-0.00232		
7.04	0.1760	0.01971	-0.00300		
7.61	0.1955	0.02051	-0.00345		
8.64	0.2292	0.02412	-0.00423	1.713	2.278
9.63	0.2740	0.03041	-0.00496	1.725	2.366
10.63	0.3167	0.03640	-0.00567	1.666	2.248
11.56	0.3572	0.04495	-0.00628	1.731	2.324
12.51	0.4001	0.05427	-0.00685	1.745	2.305
13.55	0.4445	0.06502	-0.00713	1.756	2.279
14.49	0.4843	0.07761	-0.00707	1.817	2.329
15.53	0.5269	0.09166	-0.00662	1.853	2.343
16.52	0.5708	0.10613	-0.00600	1.858	2.317
17.52	0.6188	0.12531	-0.00541	1.895	2.333
18.56	0.6609	0.14679	-0.00496	1.971	2.403
19.55	0.7067	0.16843	-0.00453	1.996	2.408
20.55	0.7554	0.19661	-0.00422	2.057	2.458
21.60	0.8029	0.22519	-0.00395	2.099	2.487
22.54	0.8478	0.25899	-0.00372	2.178	2.562
23.54	0.9013	0.29448	-0.00348	2.202	2.567
24.59	0.9455	0.32842	-0.00326	2.239	2.595
25.52	0.9785	0.36239	-0.00319	2.314	2.670
26.37	1.0268	0.39963	-0.00304	2.323	2.664

Tabel 4

KINKED WING: $\Delta C_L = 0.0815$

a_c	C_L	C_D	C_m	K	K'
-3.86	-0.2404	0.04104	0.00362		
-1.78	-0.1516	0.02398	0.00522		
-0.72	-0.0971	0.01652	0.00402		
0.32	-0.0494	0.01170	0.00319		
1.36	-0.0121	0.01166	0.00091		
2.40	0.0271	0.01099	-0.00010		
3.44	0.0677	0.01156	-0.00086		
4.47	0.1027	0.01267	-0.00205		
5.52	0.1546	0.01659	-0.00337		
6.55	0.1874	0.02099	-0.00435		
7.60	0.2354	0.02738	-0.00506	1.993	2.514
8.65	0.2908	0.03745	-0.00468	2.054	2.490
9.70	0.3432	0.04928	-0.00309	2.106	2.484
10.73	0.3764	0.05741	-0.00560	2.111	2.456
11.79	0.4352	0.07335	-0.00553	2.108	2.405
12.83	0.4744	0.08555	-0.00643	2.115	2.388
13.89	0.5388	0.10801	-0.00561	2.126	2.367
14.94	0.5860	0.12723	-0.00588	2.149	2.373
15.98	0.6361	0.14760	-0.00366	2.140	2.345
17.03	0.6858	0.17646	-0.00432	2.226	2.425
18.07	0.7276	0.19982	-0.00318	2.255	2.444
19.12	0.7745	0.22675	-0.00181	2.272	2.451
20.22	0.8254	0.26345	-0.00083	2.339	2.512
21.21	0.8725	0.29592	-0.00068	2.362	2.527
22.25	0.9106	0.32920	0.00003	2.420	2.582
23.30	0.9568	0.36414	0.00037	2.432	2.587
24.34	0.9991	0.40054	0.00030	2.460	2.609
25.37	1.0317	0.43683	-0.00023	2.521	2.670

Table 5

CURVED WING: $\Delta C_L = 0.163$

α_c	C_L	C_D	C_m	K	K'
-3.94	-0.3194	0.06699	0.00856		
-1.84	-0.2214	0.04553	0.00841		
0.26	-0.1152	0.02753	0.00812		
1.30	-0.0737	0.02238	0.00664		
2.34	-0.0308	0.01929	0.00507		
3.39	0.0160	0.01643	0.00284		
4.42	0.0560	0.01548	0.00108		
5.47	0.1000	0.01542	0.00014		
6.51	0.1409	0.01659	-0.00143		
7.53	0.1690	0.01958	-0.00263		
8.57	0.2079	0.02350	-0.00441	1.992	2.384
9.62	0.2609	0.03044	-0.00426	1.905	2.373
10.66	0.3015	0.03667	-0.00627	1.857	2.331
11.70	0.3462	0.04653	-0.00697	1.926	2.403
12.81	0.4033	0.06113	-0.00821	1.983	2.449
13.81	0.4511	0.07553	-0.00700	2.030	2.478
14.85	0.5020	0.08972	-0.00709	1.993	2.426
15.91	0.5644	0.11307	-0.00781	2.037	2.418
16.96	0.6094	0.13372	-0.00824	2.097	2.467
18.01	0.6592	0.15637	-0.00784	2.119	2.470
19.05	0.7032	0.17946	-0.00768	2.156	2.495
19.05	0.7053	0.18018	-0.00786	2.152	2.489
21.15	0.8034	0.24007	-0.00468	2.242	2.557
22.18	0.8347	0.26520	-0.00233	2.303	2.617
23.22	0.8759	0.29433	-0.00097	2.330	2.635
24.32	0.9253	0.33249	-0.00091	2.368	2.663
25.30	0.9592	0.36804	-0.00046	2.446	2.742

SYMBOLS

A	aspect ratio
c	centre-line chord
$C(x) = C = -\frac{v_z(x,0,0)}{V_\infty}$	, downwash at the centre-line
C_D	drag coefficient (= drag/$\frac{1}{2}\rho V_\infty^2 S$)
C_{D_i}	induced drag coefficient
C_{D_m}	minimum drag coefficient for cambered wing
C_{D_0}	profile drag coefficient of plane wing
C_L	lift coefficient (= lift/$\frac{1}{2}\rho V_\infty^2 S$)
C_{L_m}	lift coefficient at minimum drag
ΔC_L	camber-induced increment in C_L
C_m	pitching moment coefficient (= moment/$\frac{1}{2}\rho V_\infty^2 Sc$) about $x = 0.55\ c$
AC_P	pressure coefficient increment between upper and lower wing surfaces
$D_\nu(x)$	downwash distribution parameter
K	$= \pi A(C_D - C_{D_0})/C_L^2$, induced drag factor
K'	$= \pi A(C_D - C_{D_m})/(C_L - C_{L_m})^2$, induced drag factor
ℓ	$= -\Delta C_P$, local loading
AR	camber-induced increment in ℓ
$s(x)$	local semispan
S	plan area of the plane wing
S_w	wetted area/2
v_z	downwash velocity
V_∞	free-stream velocity
x, y, z	Cartesian coordinates with origin at apex, x downstream, y spanwise, z positive upwards
α	wing incidence from attachment condition
a_c	wing centre-line incidence

SYMBOLS (concluded)

η = $y/s(x)$

η_0 spanwise coordinate of discontinuity in v_z

η_v spanwise coordinate of leading-edge vortex

v suffix characterising downwash distributions

ϕ leading-edge sweepback angle

Φ frontal area

REFERENCES

No.	Author	Title, etc.
1	Aerodynamics Dept. staff	RAE unpublished work (1969)
2	D.A. Kirby D.L.I. Kirkpatrick	An experimental investigation of the effect of thickness on the subsonic longitudinal stability characteristics of delta wings of 70 degree sweepback. ARC R & M 3673 (1969)
3	D.L.I. Kirkpatrick D.A. Kirby	An experimental investigation of the subsonic longitudinal characteristics of five slender-wing models with gothic planforms. ARC R & M 3720 (1971)
4	Patricia J. Davies	The design of a series of warped slender wings for subsonic speeds. ARC CP No.1263 (1971)
5	P. J. Butterworth	Low-speed wind-tunnel tests on a family of cambered wings of a mild gothic planform of aspect ratio 1.4. ARC CP No.1163 (1970)
6	J. Weber	Private communication
7	J. Weber	Design of warped slender wings with the attachment line along the leading edge. ARC R & M 3406 (1957)
8	D. Küchemann	A non-linear lifting-surface theory for wings of small aspect ratio with edge separations. RAE Report Aero 2540 (ARC 17769) (1955)
9	D.L.I. Kirkpatrick	Analysis of the static pressure distribution on a delta wing in subsonic flow. ARC R & M 3619 (1968)
10	D.L.I. Kirkpatrick	Experimental demonstration of the similarity of leading-edge vortices above slender wings in subsonic conical flow. WGLR Jahrbuch, p 223-231 (1967)

REFERENCES (concluded)

No.	Author	Title, etc.
11	D.A. Kirby A.P. Cox	Unpublished work.
12	J.H.B. Smith	Improved calculations of leading edge separation from slender delta wings. RAE Technical Report 66070 (ARC 27897) (1966)
13	D.A. Kirby	An experimental investigation of the effect of planform shape on the subsonic longitudinal stability characteristics of slender wings. ARC R & M 3568 (1967)
14	C.H.E. Warren	RAE unpublished work (1957)

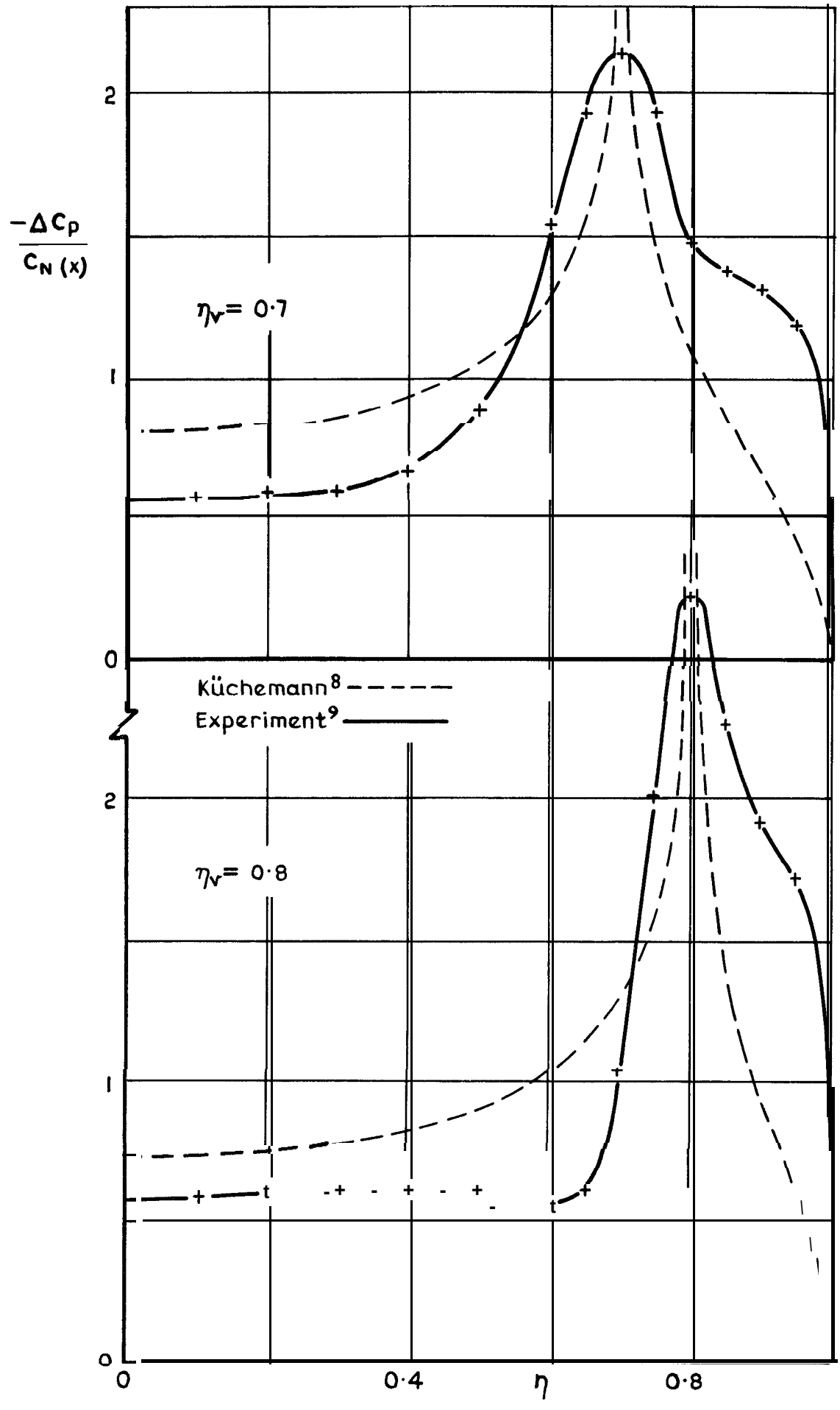

Fig.1 Comparison of theoretical and empirical loading distributions

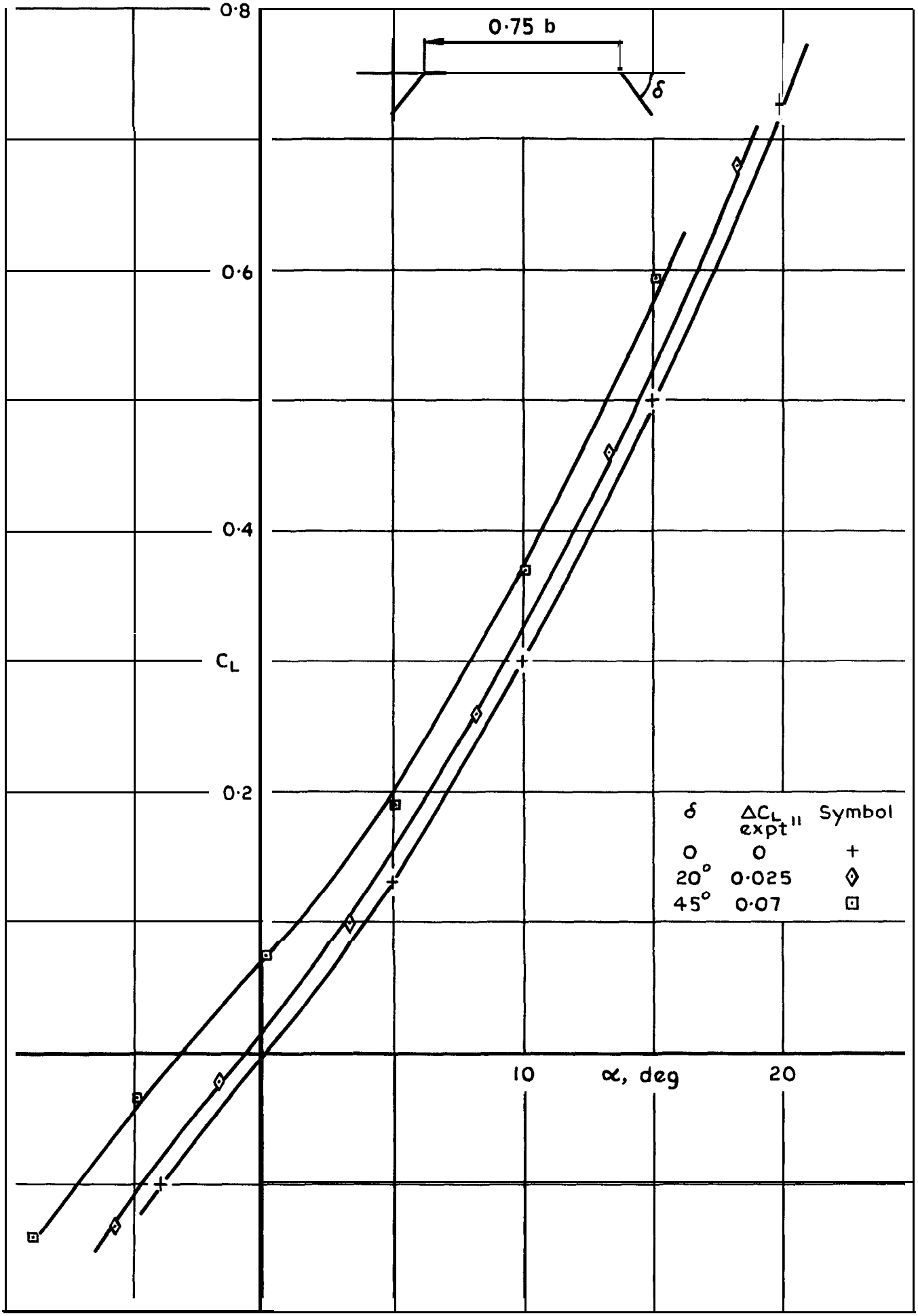

Fig.2 Lift characteristics of wings with drooped leading edges

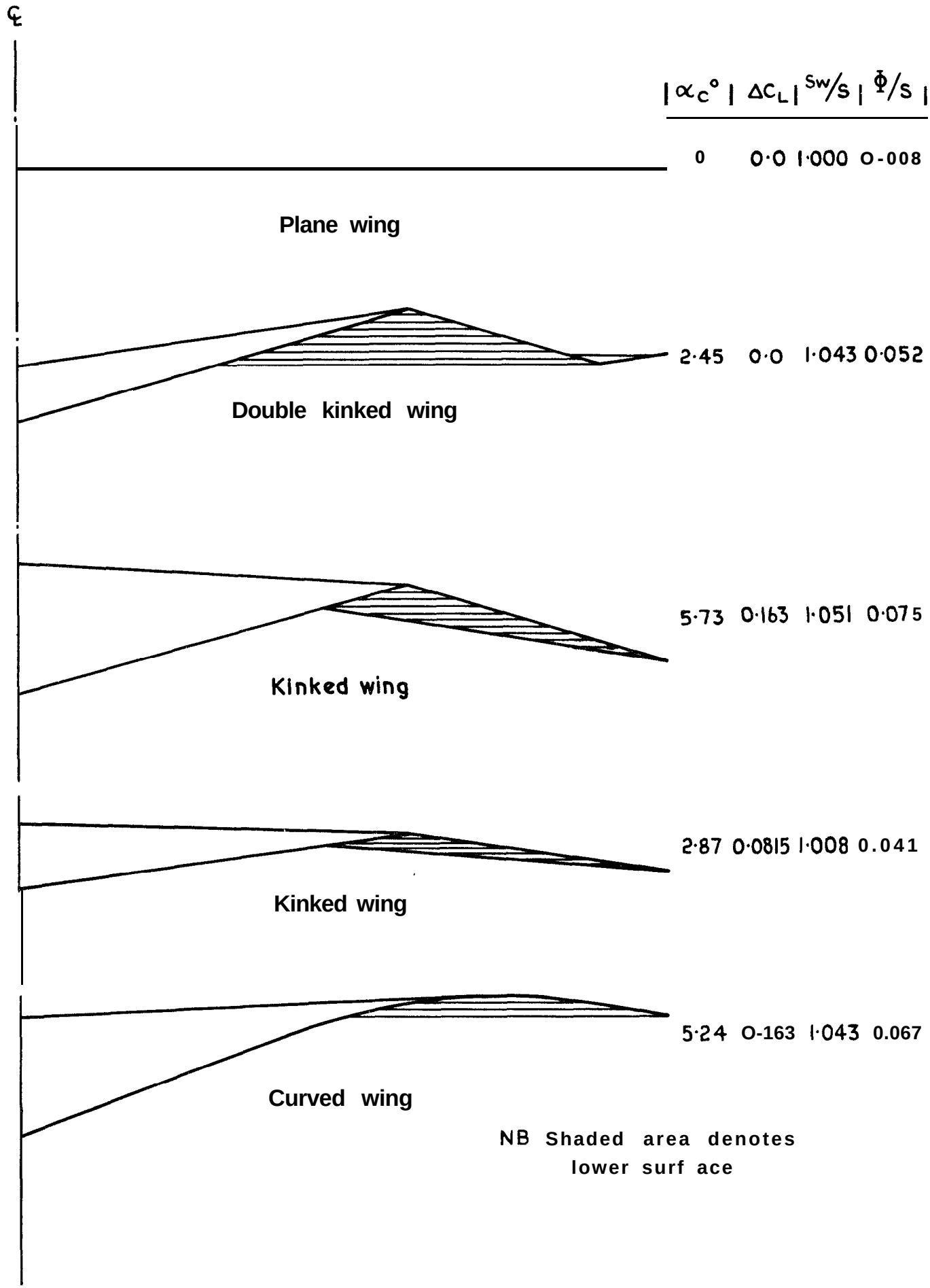

Fig.3 The 5 wings viewed from downstream (at attachment incidence)

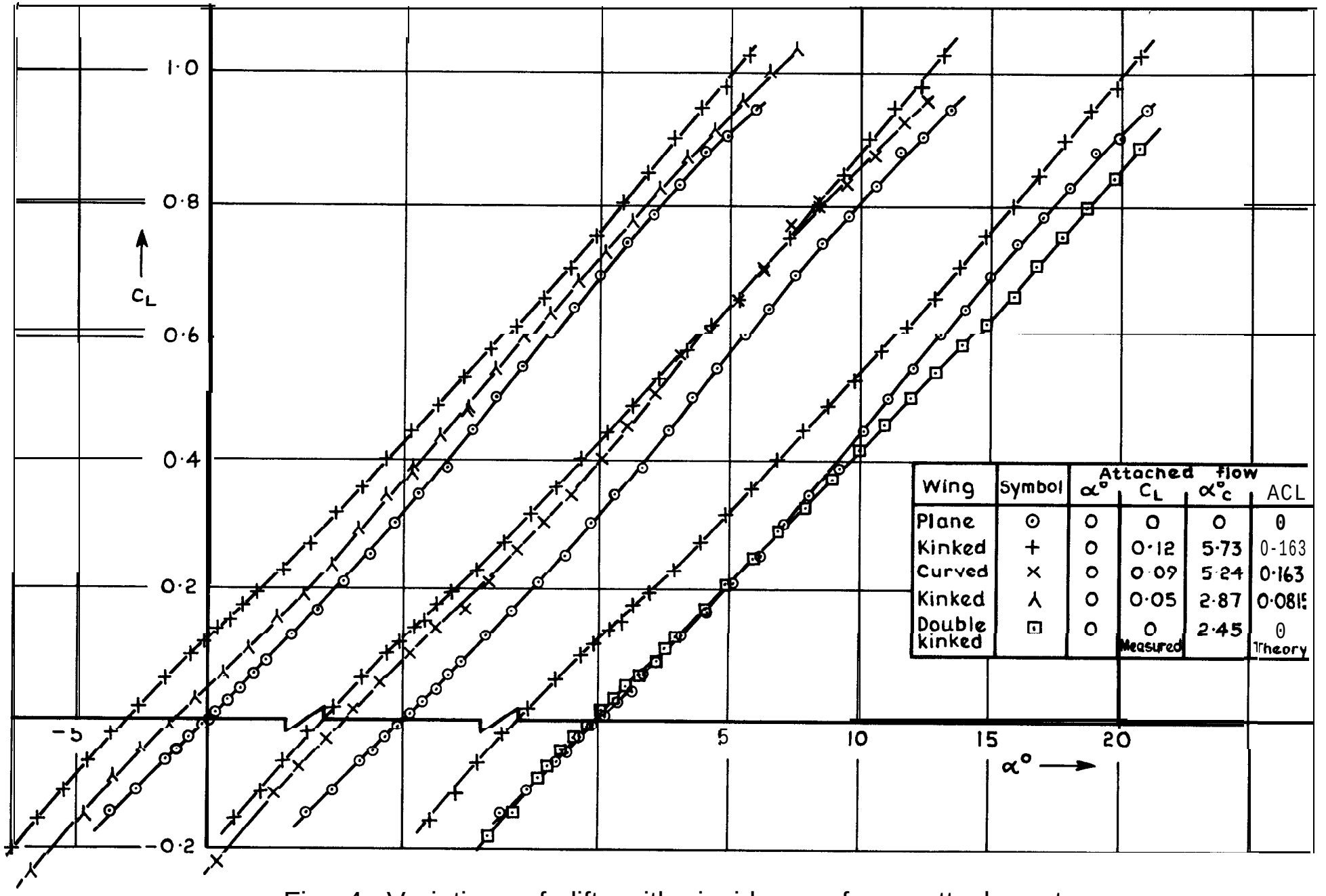

Fig 4 Variation of lift with incidence from attachment

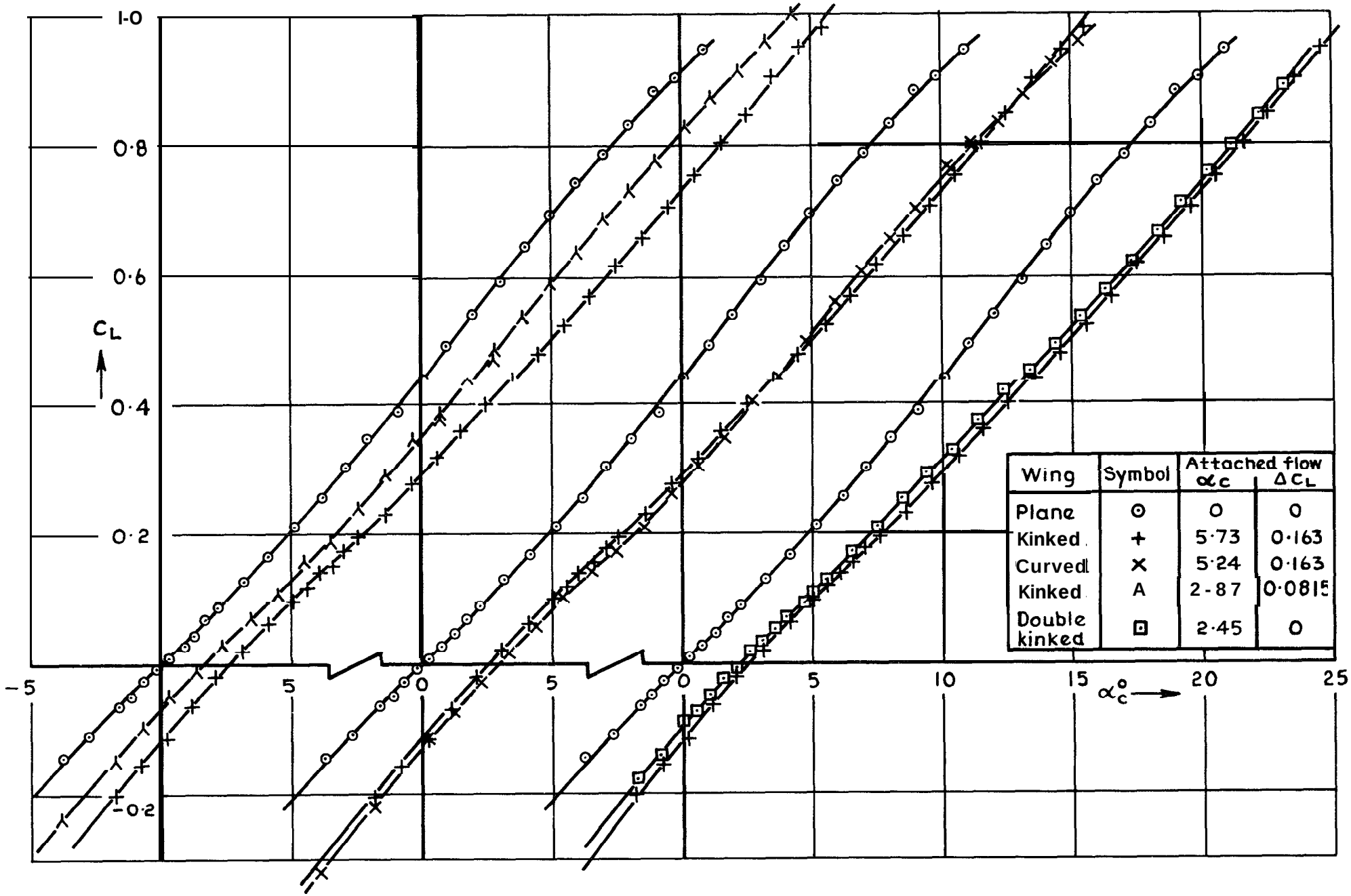

Fig.5 Variation of lift with centre-line incidence

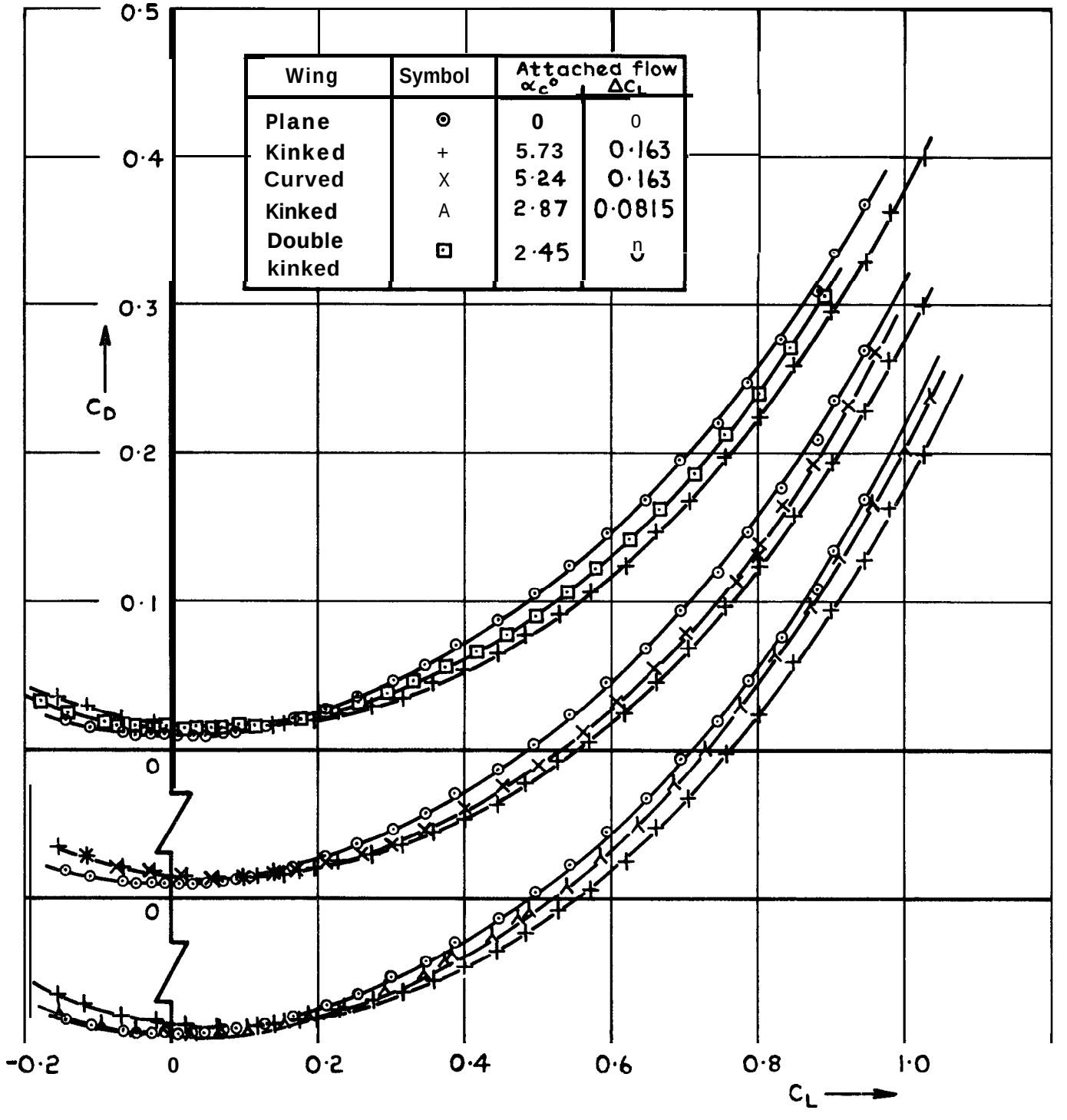

Fig. 6 Variation of drag with lift

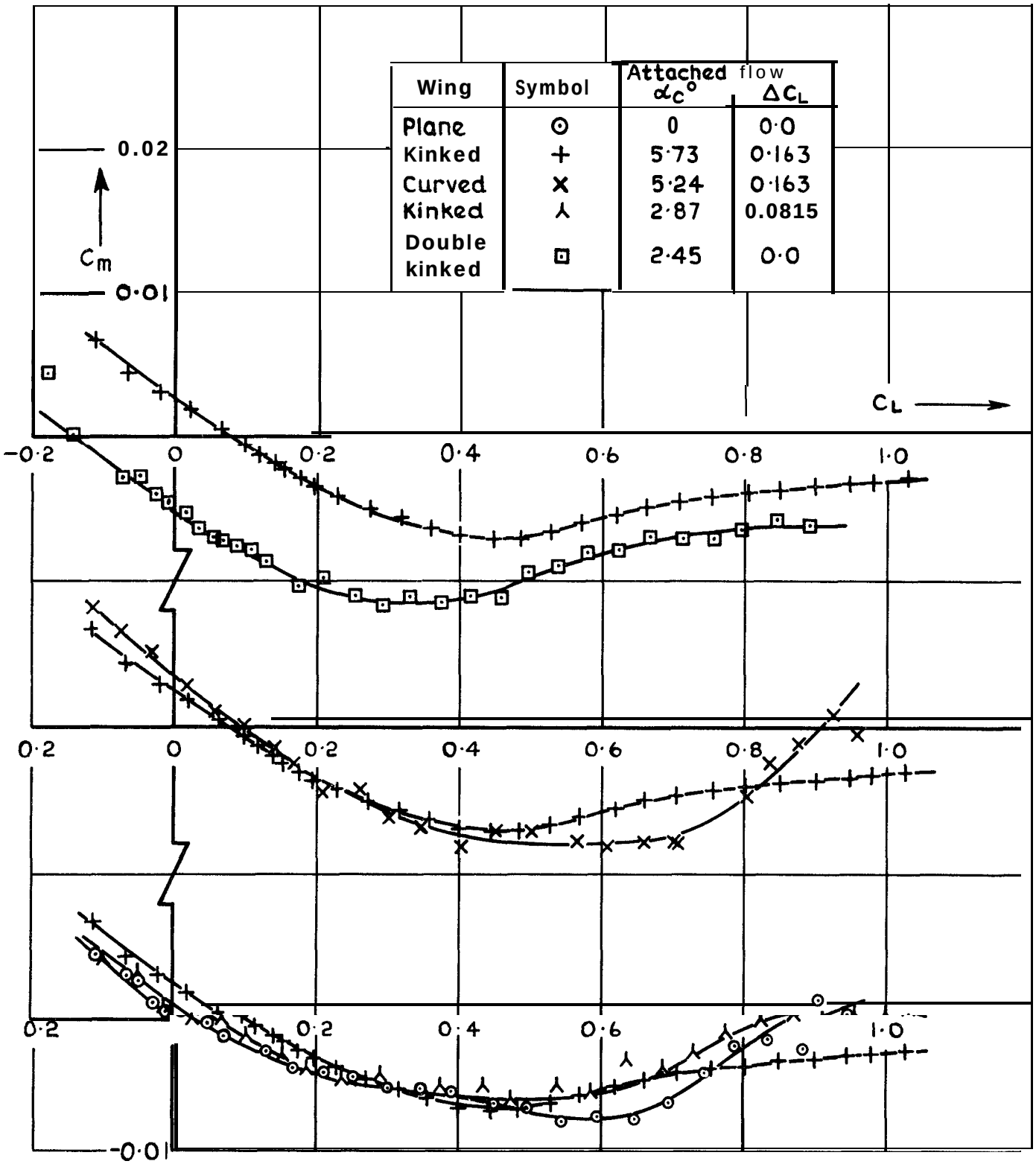

Fig.7 Variation of pitching moment with lift

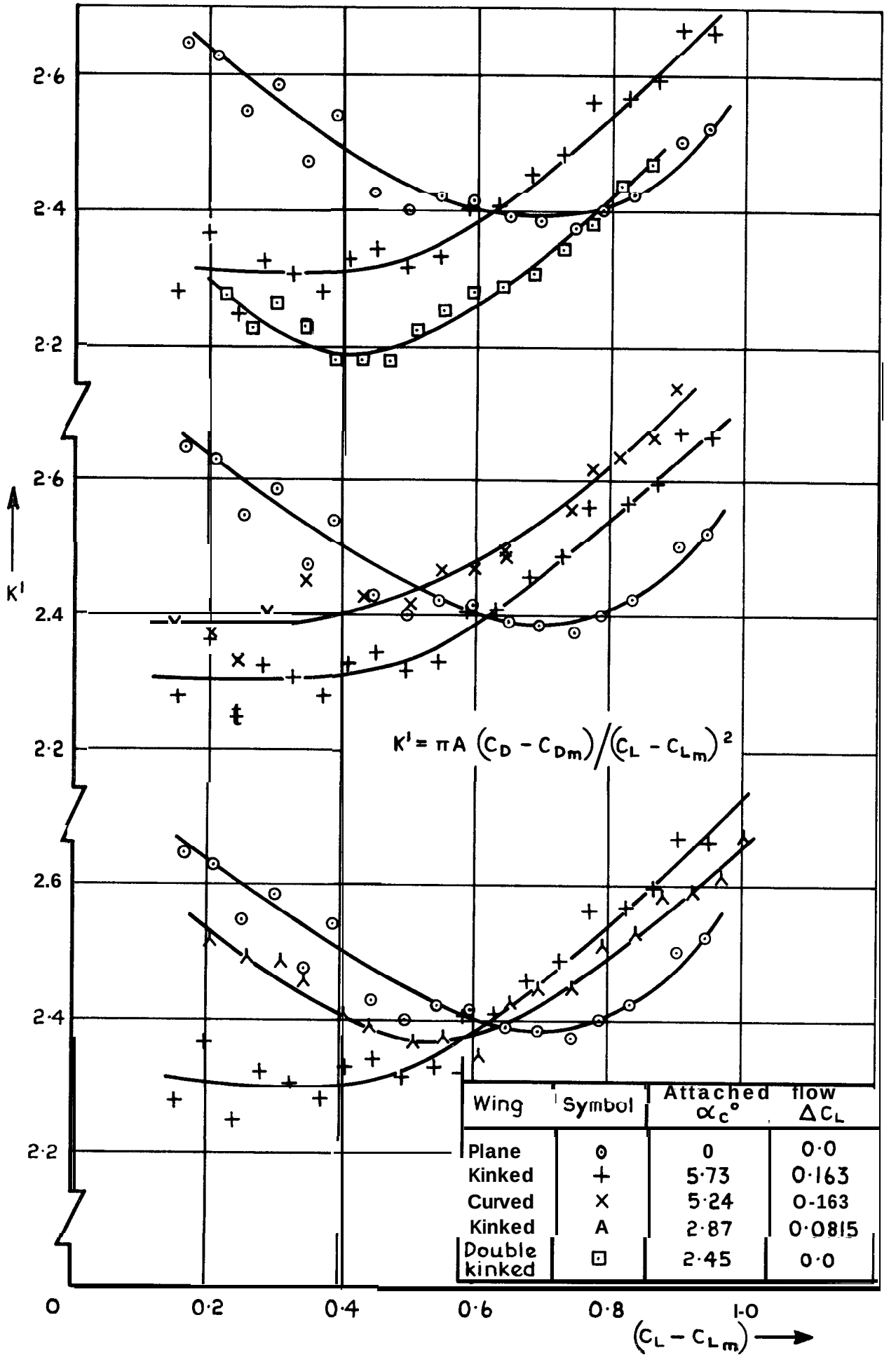

Fig.8 Variation of K' **with** lift

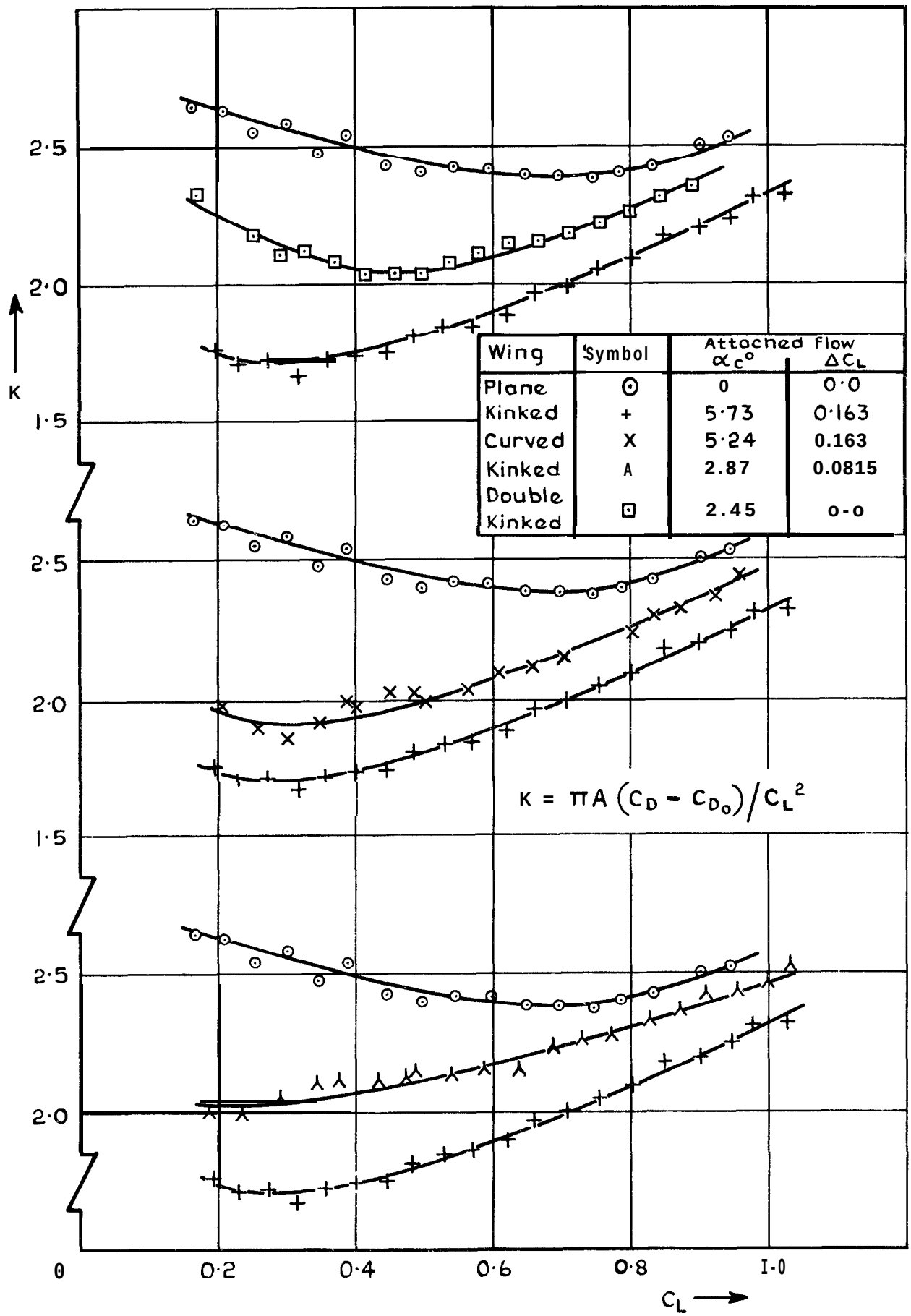

Fig.9 Variation of induced drag with lift

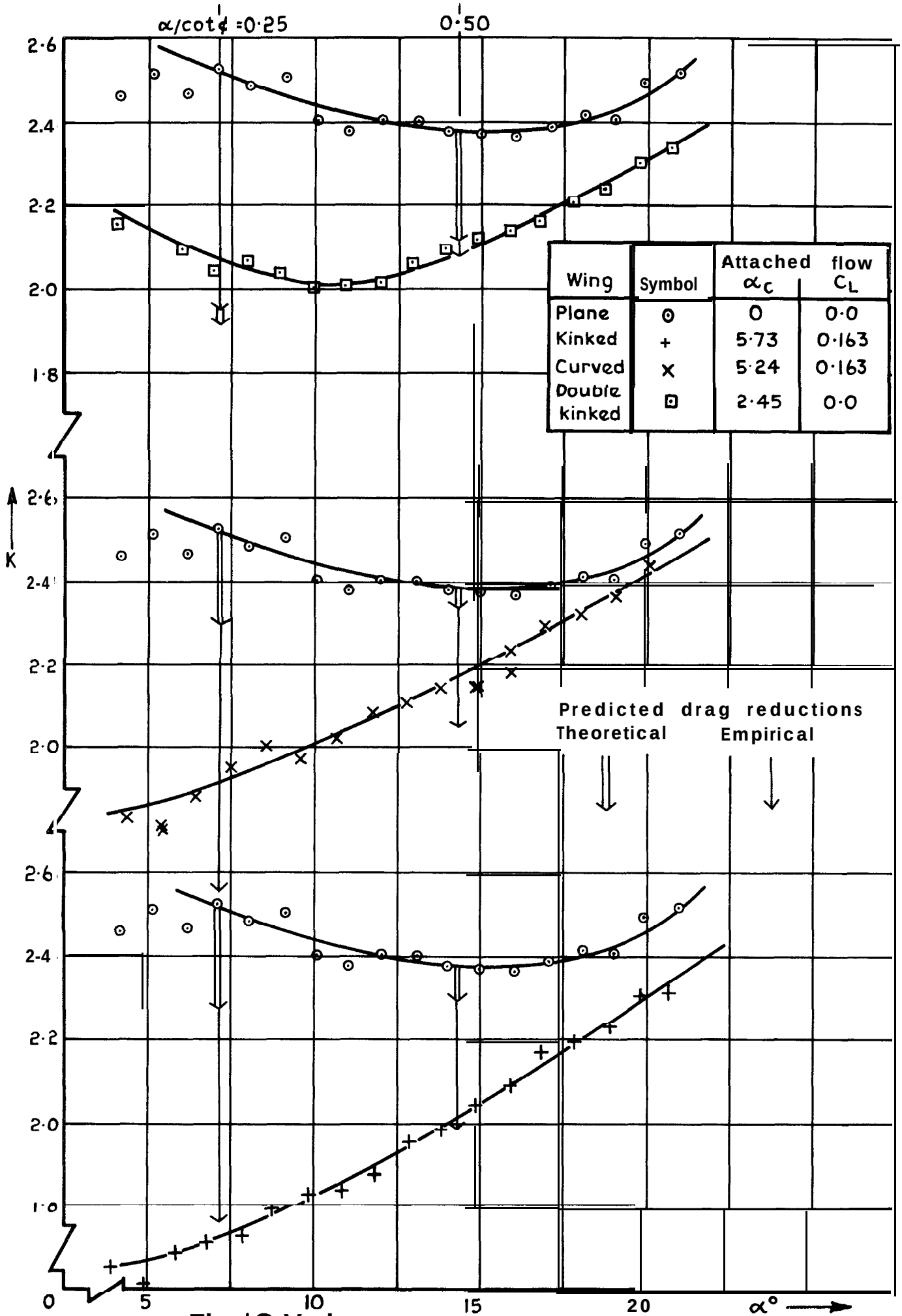

Fig. 10 Variation of K with incidence

Printed in England for Her Majesty's Stationery Office by the Royal Aircraft Establishment, Farnborough. Dd. 505376 K4 4/74.

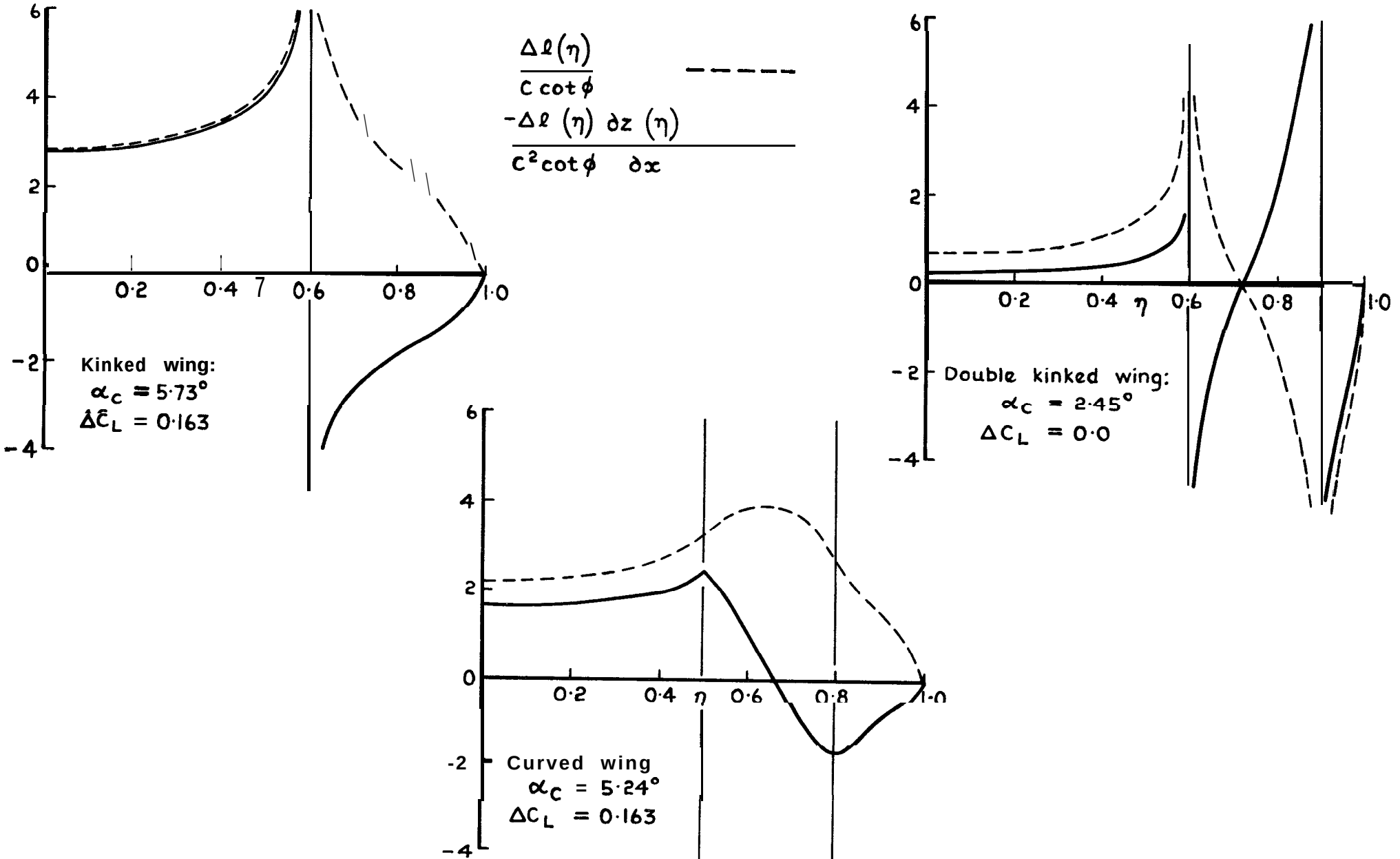

Fig. 11 Spanwise distribution of comber - induced loading

ARC CP No.1293
June 1972

Kirkpatrick, D. L. I.
Butterworth, P. J.

533.6.013.127 :
533.693.3 :
533.6.043.1 :
533.6.044.5

LOW-SPEED WIND-TUNNEL TESTS ON THE LIFT-DEPENDENT DRAG OF DELTA WINGS WITH CONICAL CAMBER

This Report describes a theoretical method of designing cambered slender wmgs to have low hftdependent drag. The results of subsonic wmd-tunnel tests on a series of thm cambered delta wings of aspect ratio 2 are presented, and the significant drag reductions achieved are discussed in relation to theoretical predicttons for the drag of cambered slender wings.

Cut here

ARC CP No.1293
June 1972

Kirkpatrick, D L. I.
Butterworth, P. J.

533.6.013.127 :
533.693.3
533.6.043.1 :
533 6.044.5

LOW-SPEED WIND-TUNNEL TESTS ON THE LIFT-DEPENDENT DRAG OF DELTA WINGS WITH CONICAL CAMBER

This Report describes a theoretical method of designing cambered slender wings to have low liftdependent drag The results of subsonic wind-tunnel tests on a series of thin cambered delta wmgs of aspect ratio 2 are presented, and the significant drag reductions achieved are discussed in relation to theoretical predictions for the drag of cambered slender wmgs.

DETACHABLE ABSTRACT CARDS

ARC CP No.1293
June 1972

Kirkpatrick, D. L. I.
Butterworth, P. J.

533.6.013.127 :
533.693.3 :
533.6.043.1 .
533.6.044.5

LOW-SPEED WIND-TUNNEL TESTS ON THE LIFT-DEPENDENT DRAG OF DELTA WINGS WITH CONICAL CAMBER

This Report describes a theoretical method of designing cambered slender wings to have low hftdependent drag. The results of subsonic wmd-tunnel tests on a series of thin cambered delta wmgs of aspect ratio 2 are presented, and the significant drag reductions achieved are discussed in relation to theoretical predictions for the drag of cambered slender wings.

Cut here

DETACHABLE ABSTRACT CARDS

C.P. No. 1293

Published by
HER MAJESTY'S STATIONERY OFFICE

To be purchased from
49 High Holborn, London WC1V 6HB
13a Castle Street, Edinburgh EH2 3AR
41 The Hayes, Cardiff CF1 IJW
Brazennose Street, Manchester M60 8AS
Southey House, Wine Street, Bristol BS1 2BQ
258 Broad Street, Birmingham B1 2HE
80 Chichester Street, Belfast BT1 4JY
or through booksellers

C.P. No. 1293

ISBN 011 470877 0

C.P. No. 1294

PROCUREMENT EXECUTIVE, MINISTRY OF DEFENCE

AERONAUTICAL RESEARCH COUNCIL

CURRENT PAPERS

SLR Temperature Measurements in the Supersonic Expansion of Nitrogen in a Shock-Tunnel

by

Michael J. Lewis and Leonard Bernstein

Queen Mary College, University of London

LONDON: HER MAJESTY'S STATIONERY OFFICE

1974

PRICE 65p **NET**

CP No.1294*
August 1973

SLR TEMPERATURE MEASUREMENTS IN THE SUPERSONIC EXPANSION OF NITROGEN IN A SHOCK-TUNNEL

- by -
Michael J. Lewis and Leonard Bernstein
Queen Mary College, University of London

SUMMARY

Temperature measurements, using the SLR method, are presented for the expansion of nitrogen in nozzles attached to a shock-tube. The measurements were made at an area ratio of 8.5 in a two-dimensional nozzle and at an area ratio of 152 in a conical nozzle. Initial conditions were such that at the entrance to the nozzles the temperature ranged between about 2500 K and 5300 K and the pressure between 1 atmosphere and 30 atmospheres.

Temporal variations of temperature were found in the nozzle flow which are similar to those previously measured at the nozzle entrance.

The apparent de-excitation rate of the nitrogen vibrational mode is up to 100 times faster than shock excitation data suggest.

*Replaces A.R.C.34 951

Contents

1. Introduction

The interest in hypersonic aerodynamics occasioned by the practicability of spaceflight has necessitated the construction of experimental facilities capable of simulating the flight conditions in one or more respects. One of the more important of these conditions is the very high total specific enthalpy associated with atmospheric flight at very high speeds. The correspondingly high temperatures, well above the melting points of structural materials, have led to the development of wind-tunnels in which the high enthalpy flow is of very short duration, so that only a minimum amount of heat transfer takes place to the structure of the tunnel. Among these devices is the reflected-shock tunnel, in which a convergent-divergent nozzle is fed from a reservoir of high enthalpy gas generated by the passage of a normal shock-wave and its reflection from the end wall of a shock-tube.

The ideal behaviour of such a tunnel is fairly well understood (see, for example, Glass & Hall, 1959). However in practice departures from this ideal behaviour arise as a result of "real-gas effects"; viscous friction, heat transfer, turbulent mixing and deviations from thermal equilibrium at the molecular level all play a part.* Many of these effects have been investigated both experimentally and theoretically, and while they are thought to be understood in large measure, the complexity of the flow processes has meant that accurate predictions of the state and duration of the flow of test gas cannot be made. In essence then, each shock-tunnel needs to be calibrated. Of course this is true of any wind tunnel, but the high specific enthalpy of the shock-tunnel flow, the way in which this flow is generated and its short duration make the calibration more difficult than with conventional wind-tunnels.

An earlier report (Lewis & Bernstein, 1973) described some experiments designed to ascertain the thermodynamic state and steadiness of the reservoir gas behind the reflected shock in the small shock tube at Queen Mary College, the cross-section of which is 38.1 mm square.

---

* Caloric and thermal imperfections may be readily taken into account and are not regarded as affecting the "ideal" behaviour, a term used to denote the behaviour under conditions when transport phenomena depending upon molecular collisions are negligible.

The results showed that the reservoir gas was not in as uniform a thermodynamic state as is desirable, nor is it free of disturbances for as long as ideal theory predicts. Similar results have been reported by other workers (for example Lapworth & Townsend, 1967).

The present report describes some experiments designed to examine the effects of this lack of ideality on the hypersonic flow issuing from a convergent-divergent nozzle. Two different nozzles have been tested. The first is a two-dimensional nozzle mounted within the confines of the shock-tube. This is the same nozzle described earlier (Lewis & Bernstein, 1973), the measurements then relating to the entrance region ahead of the convergence. On this occasion temperature measurements in the diverging portion are described. The second nozzle is a conical one, with provision for measuring stations at several positions along the divergence, at much larger area ratios than are available with the two-dimensional nozzle. In the event measurements were only possible at one station.

The thermodynamic behaviour of the expanding nitrogen - the test gas used - is perhaps the least well understood of the processes which take place in a shock-tunnel operating at moderate pressures. In the hot "stagnant" gas in the reservoir, the pressure is usually sufficiently high for thermodynamic equilibrium to exist. Thus the temperature associated with the vibrational excitation of the molecules is equal to that of the active modes. (We are assuming here that the specific enthalpy is not so great that dissociation occurs, but a similar argument to that which follows may be applied to chemical relaxation.) When the hot gas expands into the nozzle, the pressure, density and "temperature" fall. The fall in density implies a reduction in the rate of molecular collisions, and in consequence the mechanism whereby the temperatures associated with the vibrational and active modes become equal is less effective. The "vibrational temperature" freezes and energy remains locked in the vibrational motion of the molecules, while the internal energy of the active modes - translational and rotational - is converted into the directed kinetic energy of mass motion along the nozzle.

Now the relaxation rate has been measured for vibrational excitation of the gas behind a shock-wave. Such data were obtained in this shock-tube for nitrogen , and these compared well with those of other workers (Lewis & Bernstein, 1973). In theory, with these data and the equilibrium constant, it should be possible to estimate the value at which the vibrational temperature will "freeze" for any given reservoir conditions and nozzle. Such estimates prove to be seriously in error, the apparent relaxation rate being much faster in the expanding, de-excitation environment than one would infer from the excitation data. The reasons for this remain somewhat obscure (see Hurle, 1971 for an excellent discussion). In consequence the nozzle flow must be calibrated in the gross sense to determine the average thermodynamic state, as distinct from the possible variations with time which may exist in addition to those from point to point in the test section.

Such a calibration is presented in the following sections. In the light of the foregoing remarks, attention has been concentrated on the measurement of temperature. In particular the spectrum-line reversal technique has been used with sodium as the seed element, it being assumed that the temperature at which the sodium line-reversal takes place is that corresponding to the vibrational temperature of the nitrogen.* In discussing the results in detail, emphasis is placed upon correlating the measurements with those made in the reservoir, and it may be found convenient to have more of those results (Lewis & Bernstein, 1973) to hand than are included here.

The measured temperatures are also compared with the "frozen" vibrational temperatures predicted using a computer model of the expansion with several relaxation equations. These equations have the temperature dependence of the shock-excitation data, but contain a constant factor λ, which represents the apparent enhancement of the relaxation rate during de-excitation.

---

* Resonance between the sodium electronic excitation and the 7th vibrational level of the nitrogen is believed to occur. However doubt has recently been expressed (Hurle, 1971) that the vibration energy distribution is Boltzmann-like in a nozzle flow.

2. The shock-tunnel and its operating conditions

The shock-tube used to generate the high enthalpy gas has a channel section some 4.86 m in length the bore of which is 38.1 mm square. This channel section is fabricated from bars of duralumin and seals are provided so that it may be operated at sub-atmospheric pressures, a two-stage rotary vacuum pump being used to evacuate it. The steel driver-section is 1.22 m long and has a bore of diameter 76.2 mm. The Melinex diaphragms are preloaded into a special block so as to reduce to a minimum the replacement time, and consequently the time during which the tube is open to atmosphere. Diaphragm rupture is initiated using a spring-loaded plunger. A more detailed description of the basic shock-tube and its auxiliary equipment is given by Bernstein (1963) and some of the subsequent modifications are described by Ackroyd (1964). The original shock passage detectors and their associated electronic amplifiers have been replaced by the improved equipment described by Bernstein & Goodchild (1967).

The shock-tube may be converted for use in the shock-tunnel mode in one of two ways. Between the downstream end of the shock-tube and the dump-tank, there may be placed either an extension to the shock-tube channel or a conical nozzle. The extension box has been designed as a special test section for the shock-tube, and as well as having three pairs of large diameter portholes in which windows may be mounted, it also has provision for mounting models within the shock tube flow. Such models are held in position by dovetails on the upper and lower walls of the tube, and for one of the sets of experiments described here the "model" consisted of a two-dimensional nozzle formed by two steel inserts, as shown in figure 1. Station m, where the measurements were made, is 5.386 m from the main diaphragm. The area ratio of this nozzle is small (of order 10) and so it is not necessary to provide an initial pressure difference across it to aid starting. The dump-tank, nozzle and channel are all initially at the same pressure, and the nozzle driving pressure is provided by the difference between this pressure and that behind the shock which is reflected from the entrance to the nozzle.

The conical nozzle is of steel, and the interior surface is coated with an epoxy-based paint to reduce outgassing at the relatively low initial pressure needed to ensure that the nozzle will "start".

The throat section of this nozzle is 9.53 mm in diameter and it is situated about 4.9 m from the main diaphragm. A thin Melinex diaphragm is clamped at the throat section to support the initial pressure difference between the nozzle and the channel; this diaphragm vapourises rapidly upon shock reflection. Several measuring ports are provided along the expansion cone, their positions and other relevant dimensions being shown in figure 2.

The shock-tube was operated with high pressure hydrogen driving shocks into nitrogen. The nitrogen test gas was of commercial quality, but was specifically free of oxygen. Before charging the shock tube each section was evacuated. The driver section was evacuated to a pressure below 1 torr, the channel section to a value below 0.1 torr, and the conical nozzle to a pressure of about 0.01 torr, its working pressure. As mentioned earlier the time during which the shock-tube was open to atmosphere was kept to a minimum in order to minimise the impurity level of the test gas. However no special precautions were taken to prevent the back-streaming of oil vapour from the vacuum pumps.

The other main source of impurity is associated with the temperature measuring system. However, by using sodium azide, the number of impurity atoms was minimised. The single-source , sodium line-reversal system is described in detail by Lewis & Bernstein (1973).

The range of incident shock Mach number at which tests were carried out was 4.6 to 7.6, giving nominal temperatures T_0 at the nozzle entrance between about 2500 K and 5300 K. The initial pressures in the shock tube were varied so that the pressure p_0 in the reservoir at the nozzle entrance ranged between 1 atmosphere and 30 atmospheres. The initial pressure in the channel was measured by two Wallace & Tiernan gauges covering different ranges, and the shock velocity was determined by timing the shock passage between stations a short distance upstream of the nozzle entrance using deci-microsecond chronometers. The effective shock velocity at reflection was inferred from these wave velocity measurements and the shock attenuation data of Bernstein (1963), obtained for the same shock tube.

3. Measurements in a two-dimensional nozzle

Measurements of vibrational temperature T_V were made, through flush-mounted windows, at station m which was centred downstream of the throat at a local nozzle area to throat area ratio of 8.5 . The photomultiplier signals from the line-reversal system were displayed on an oscilloscope and recorded on Polaroid film. Four typical variations of T_V with time t are shown in figures 3 and 4 together with two representative oscillograms. The size of the data points is intended to indicate the estimated uncertainty* in temperature and time, the latter being measured from the (estimated) time of arrival of the incident shock at the nozzle entrance. On the oscillogram "a" indicates an absorption of light from the calibrated background source, a filament lamp at an effective brightness temperature of $\overline{T}_L$. The arrow "e" indicates emission from the sodium seed atoms in the nitrogen test gas. S_N marks the arrival at the measuring station of the starting wave process. The nozzle entrance conditions, specified by T_o and p_o are inferred from the previous calibration of the region behind the reflected shock-wave.

Two significant points C_N and D_N are marked on each temperature history to indicate the sudden changes in T_V which occur. Temperatures T_{CN} and T_{DN} together with the corresponding times t_{CN} and t_{DN} at which they occur are defined for these points. Although these values of time for the present measurements are not directly comparable with those in the region behind the reflected shock (the former are from an Eulerian point of view, while the latter are essentially from a Lagrangian viewpoint), the similarity between the temporal variations of T_V and T_o is evident. It seems reasonable therefore to associate the temperatures T_{CN} and T_{DN} with TC and T_D respectively, and the latter may be estimatedfrom the earlier calibration at the nozzle entrance.

---

* At the higher values of the reservoir temperature range, dissociation of the nitrogen occurs absorbing large quantities of energy from the active and vibrational modes. Dissociation depletes the population of the upper vibrational energy levels which are repopulated from the lower levels. Thus dissociation effectively reduces the vibrational temperature measured by the present line-reversal method.

At a time earlier than t_{CN} a rather higher temperature is evident than would be expected from the temperature variation at the entrance to the nozzle. Two possible reasons for this may be put forward. Sodium atoms are present in this nozzle before the incident shock arrives at the entrance. When the starting waves process the gas initially at the measuring station, a temperature rise occurs which is detected by the line-reversal system. This temperature may be quite high because the shock strength increases in the converging portion of the nozzle, though of course it will attenuate in the diverging section. The net effect is uncertain and vibrational relaxation behind the shock front probably also needs to be taken into account. An alternative explanation is that the signal is "false", resulting from a scattering of light into the emission beam from the high temperature gas at the nozzle entrance. This "pre-emission" signal would be reduced as the scattered light is absorbed by the relatively cooler sodium atoms in the nozzle flow and in the boundary layer on the nozzle walls.

Davies (1965) has demonstrated that as a result of the interaction which takes place between the reflected shock and the boundary layer growing behind the incident shock, cold driver gas - hydrogen in this case - is introduced into the nozzle entrance region and thus into the nozzle. It is believed that the rapid fall in temperature after t_{DN} is the result of this cold hydrogen arriving at the measuring station.

As some indication of the duration of high enthalpy flow the times t_{CN} and t_{DN} are plotted in figure 5 as a function of the shock Mach number at the nozzle entrance. Curves for the corresponding times t_C and t_D at the nozzle entrance are also shown for comparison.

It is possible to obtain estimates of the characteristic vibrational relaxation time τ for de-excitation from these measurements. The computations of Wilson, Schofield & Lapworth (1967) indicate that within the range of reservoir conditions tested, the vibrational energy mode should be frozen upstream of the measuring station m. Thus the measured reversal temperatures which are assumed to correspond to the vibrational temperature are no direct guide to the energy content of the active modes; they represent the frozen vibrational temperature.

Theoretical estimates of this frozen vibrational temperature T_F, for a particular nozzle and given initial conditions may be obtained by solving the one-dimensional flow equations simultaneously with a rate equation for vibrational relaxation. Wilson and his colleagues (1967) have carried out such calculations for a range of reservoir conditions and a two-dimensional nozzle having a throat height r^* of 2.54 mm and slightly curved walls, the semi-angle θ_N near the throat region being about 12.5'. They use the equation (with $\lambda = 1$)

$$\frac{\tau p}{\mu s \ atm} = \frac{1.1 \times 10^{-5}}{\lambda} \left(\frac{T}{K}\right)^{\frac{1}{2}} \exp\left\{\frac{154}{(T/K)^{1/3}}\right\}$$

for the relaxation time together with the Landau-Teller rate equation, where A = 1 corresponds to the measured rates in a shock-excited environment and $\lambda = 10$ implies a rate ten times faster, on average, than those measured.

The differences between their nozzle and that used in the experiments reported here may be taken into account by means of the similarity parameter (Campbell, 1963)

$$\Lambda = \frac{r^* p_o \lambda}{\tan \theta_N} \quad .$$

It is assumed that T_F is a function only of Λ and that differences in r^* and θ_N may be compensated by adjustment of the reservoir pressure po for a fixed value of A.

Using the results of **Wilson, Schofield** and **Lapworth** (1967) in this way and taking A = 1, values of T_F corresponding to the present tests have been estimated. The ratios of the measured temperatures T_{CN} and T_{DN} to those values of T_F are plotted in figure 6 as a function of the stagnation temperature T_o. The fact that all these ratios are less than unity implies that $\lambda > 1$ and that de-excitation proceeds faster than excitation measurements would suggest. The procedure was repeated with $\lambda = 10$, but the ratios of measured to estimated temperature were

still below one. Unfortunately the range of computations presented by Wilson and his co-workers is not sufficient to include $\lambda = 100$ for the experimental conditions reported here, but extrapolation suggests that de-excitation of the vibrational mode proceeds about two orders of magnitude faster in this nozzle than expected from shock-excitation measurements.

The data of other workers (see Hall & Russo, 1967) are also indicated in figure 6. Agreement between their data and that reported here would be implied were the latter to fall more or less within the shaded area. Direct comparison is not strictly justifiable because of the different correlation equation they use for the excitation data. However it is expected that differences arising from different nozzle geometries and stagnation pressures may be largely eliminated by plotting the ratio of measured to calculated temperature (Hall & Russo, 1967).

4. Measurements in a conical nozzle

Temperature measurements were also made through windows mounted in the removable inserts of station AA' of the conical nozzle. The local geometric area ratio at this station is 152. The early attempts to obtain measurements were unsuccessful, a very poor signal-to-noise ratio resulting from the thick boundary layer growing on the nozzle wall through which the light had to pass. The windows, originally almost flush with the wall, were remounted so as to extend through the boundary layer as illustrated in figure 7. With this "skimmer" technique satisfactory results were obtained, but the noise level remained fairly high, largely because the equipment needs to be operated at high sensitivity when the gas density is low. Even with the "skimmer" technique attempts to obtain measurements at station CC' in the nozzle failed because the signal-to-noise ratio was so poor. Several complementary measurements of static pressure in the nozzle were made using a Queen Mary College, type H transducer (Goodchild & Bernstein, 1972) mounted

at station B. Signals were displayed on a cathode ray oscilloscope and recorded on Polaroid film.

Some typical variations of vibrational temperature with time are shown in figures 8 to 11 together with representative oscillograms. The vertical bars on the data points indicate the uncertainty in the measurements which results largely from the noise, evident on the oscillograms. Again time is measured from the estimated time of arrival of the incident shock at the entrance to the nozzle. The nomenclature used in these figures is similar to that used for the two-dimensional nozzle with the addition of a point J_N which marks the first arrival at AA' of hot gas from the reservoir. Because very few sodium atoms are present in the nozzle prior to shock arrival, the starting wave system was not detected by the sodium line-reversal system. The abnormally high "emission" signal at the beginning of each oscillogram are almost certainly caused by scattered light. The influence of the varying conditions in the reservoir is again clear and once more the sharp fall in temperature after time t_{DN} is believed to be caused by the premature arrival of cold hydrogen at the measuring station.

A static pressure record, taken at station B is reproduced as figure 12. Because of the transducer ringing, resulting from vibration of the shock-tunnel structure, only four "reasonable" records were obtained. Although this precludes quantitative measurements from being made, the influence of the varying reservoir conditions is fairly clear, and so is the arrival of the starting shock, labelled S_N, at station B.

As an indication of the duration of the (albeit unsteady) high enthalpy flow, the times t_{CN} and t_{DN} are plotted in figure 13 as a function of the incident shock Mach number W(XT) in the shock-tube. For comparison curves for the corresponding times t_C and t_D at the nozzle entrance are also shown. The time t_{JN} at which hot gas from the reservoir first arrives at the measuring station is also shown, and may be compared with time t_{SN}, the time of arrival of the starting wave at station AA', inferred from the pressure measurements at station B.

Values for the frozen vibrational temperature TF were calculated for this nozzle using the computer programme of Wilson, Schofield and Lapworth (1967) and the relaxation-time equation of Section 3 which is based upon a correlation of shock-excitation data (Erickson 1963) which accorded quite well with the measurements reported earlier for this shock-tube (Lewis & Bernstein, 1973).. Corrections for the boundary-layer growth on the nozzle wall were made by estimating a typical value of the displacement thickness, modifying the nozzle angle accordingly and using the similarity parameter Λ as before. The corrections were small, so that a more elaborate approach was unjustified in view of the uncertainties in the measurements.

Some of the measurements have been grouped into two sets: one group is characterised by a stagnation temperature of approximately 3300 K, the other group by a common reservoir pressure of 13 atmospheres. Figures 14 and 15 show these two sets of data together with the theoretical predictions for various values of the relaxation enhancement rate parameter A . The ratio of measured to calculated frozen vibrational temperature (for $\lambda = 1$) is also shown in figure 16.

The scatter in the data arises partly from uncertainties in the measurements in the nozzle and partly from uncertainties in the stagnation conditions. An accurate assessment of the relaxation rate in this nozzle, cannot therefore be made. It would appear from figure 14 that the effective relaxation rate diminishes with increasing reservoir pressure. On the other hand figure 15 suggests that the effective rate increases with increasing T_0, although the results at high stagnation temperature are subject to greater uncertainty because of the possibility of some dissociation having occurred in the reservoir.

For this nozzle the effective enhancement rate λ would appear to be about 20 on average. Again a direct comparison with the data correlated by Hall & Russo (1967) is not justifiable because of the different basis upon which they estimate T_F . Had their rate equation been used for the shock-excitation data, a larger value of λ would have been obtained, comparable with the value of 70 that they quote.

5. Concluding remarks

Temperature measurements using the sodium time-reversal technique have been made in nitrogen expanding quasi-steadily in two separate convergent-divergent nozzles attached to a shock-tube. These measurements were made at a geometric area ratio of 8.5 in a two-dimensional nozzle and 152 in a conical nozzle. The initial shock-tube conditions were such that at the entrance to the nozzle the pressure ranged from 1 atmosphere to 30 atmospheres and the stagnation temperature from about 2500 K to 5300 K, the system being used as a reflected shock tunnel.

The variations in measured temperature in the expanded flow follow fairly closely those measured previously at the entrance to one of the nozzles, albeit on a slightly different time scale (Lewis & Bernstein, 1973). The duration of high total-enthalpy flow is about 0.3 ms. Over this period, the measured temperature, which is associated with the vibrational temperature of the nitrogen, varies by approximately 10%. The ideal behaviour of a shock-tunnel as characteriseg by the "tailored-interface" mode of operation was not apparent. The variations in temperature during the "steady" flow period are thought to be due to the finite extent of the "interface" between the driver and driven gas in the shock tube (Lewis & Bernstein, 1973) so that there are always waves of finite strength reflected from the interaction between this region and the reflected shock. The premature termination of the hot flow is believed to result from the arrival at the test station of cold driver gas which also emanates from the shock-mixing region interaction. The cold gas in the boundary layer, having a momentum differing from that in the core flow is not brought to rest by the reflected shock as is required for ideal operation in the tailored-interface modes (Davies, 1965).

Further non-idealities arise in shock-tunnels operated at moderate pressures because of the finite relaxation time of the vibrational mode(s) of polyatomic molecules such as nitrogen. Usually the gas in the reservoir region of a shock-tunnel is of sufficiently high density for thermal equilibrium to exist there. Upon expansion the energy in the vibrational mode is frozen, but the frozen vibrational temperatures of nitrogen appear to be lower than shock-excitation relaxation rates would

suggest. The de-excitation rates appear to proceed about 20 to 100 times faster than the excitation rate does at the same pressure and temperature.

One suggestion which has been put forward in explanation is that as the gas departs further from equilibrium the distribution of energy in the vibrational mode becomes less Boltzmann-like. Since the sodium line-reversal technique which was used measures essentially the "temperature" of only one vibrational level, it does not give a result representative of the vibrational energy as a whole. Hurle (1971) discusses this explanation further together with the results of other workers who use different measuring techniques with similar anomalous results for nitrogen (see, for example, Russo & Watt, 1968).

Another explanation involves the effects of impurities; in particular highly mobile hydrogen atoms have been suggested as having a catalytic effect. Unless elaborate precautions are taken, the impurity level is difficult to control. Systematic tests by Russo (1966) over a range of hydrogen compound concentrations from 10^{-4} to 3×10^{-3} show little effect on the de-excitation rate except for concentrations above 10^{-3}. However Russo was careful to draw no conclusions for concentrations below 10^{-4}. In the present experiments sources of hydrogen are manifold. Hydrogen was of course used as the driver gas, and in spite of evacuation of the shock-tube prior to loading with test gas, some hydrogen will have remained. Again the mechanical vacuum pumps are a source of hydrocarbon oil vapours, which may "back-stream" into the test gas, since no "cold-trap" was used. Such hydrocarbons are readily stripped of hydrogen atoms in the high temperature environment of the doubly shock-processed gas at the entrance to the nozzle. The hydrogen bond is such that the typical characteristic dissociation temperature ($\theta_D = D/k$) is about 53 000 K, so that appreciable dissociation, 0.1% say, will occur at temperatures of about 2 000 K, at pressures of order 1 atmosphere.

The present results do not allow us to distinguish between these explanations and the reasons for the anomaly remain obscure, Until a satisfactory explanation is forthcoming, tests in hypersonic high enthalpy streams will always be attended by some uncertainty as regards the state of the undisturbed flow.

Acknowledgments

This work was supported by the then Ministry of Technology under an extra-mural agreement, and one of us (M.J.L.) would like to express his gratitude for a maintenance grant during the course of the project of which this forms a part.

Thanks are also extended to Dr. D. Schofield of the National Physical Laboratory who kindly used his computer programme to solve the equations for the nozzle flow.

Nomenclature

p	pressure
t	trace (real) time
t_K	time to point K (see suffices)
T	temperature
T_K	temperature at point K (see suffices)
T_V	measured vibrational temperature
$\overline{T}_L$	lamp brightness temperature
$W(X_T)$	incident shock Mach number at nozzle entrance

Suffices

o	nozzle entrance conditions
1	initial channel conditions
K	points on measured data :
	K = C, D for nozzle entrance measurements
	OR K = C_N, D_N, S_N, JN for nozzle flow measurements
	calculated frozen value

References.

Ackroyd, J.A.D. 1964 Ph.D. Thesis, University of London.

Bernstein, L. 1961 "Some measurements of Shock-Wave Attenuation in Channels of Various Cross-Sections". A.R.C. R. & M. 3321.

Bernstein, L. & Goodchild, R.O. 1967 "High-sensitivity piezoelectric transducer for wave velocity measurements in shock-tubes". Rev. Sci. Instr. 38, p.971.

Campbell, W.F. 1963 "Hypersonic Nozzle Flow with Vibrational Non-Equilibrium". Von Karman Institute, Course Note 33, p. D-3a.

Davies, L. 1965 "The Interaction of the Reflected Shock with the Boundary Layer in a Shock Tube and its Influence on the Duration of Hot Flow in the Reflected Shock Tube". A.R.C. C.P. 880 and C.P.881

Erikson, W.D. 1963 "Vibrational nonequilibrium flow of Nitrogen in Hypersonic Nozzles". NASA TN-D-1810.

Glass, 1.1. & Hall, J.G. 1959 "Shock Tubes" (Handbook of Supersonic Aerodynamics, Section 18) NAVORD Rep. 1488 (Vol. 6)

Goodchild, R.O. & Bernstein, L. 1969 "The design of high sensitivity pressure transducers for use in shock-tunnels". A.R.C. C.P. 1219.

Hall, J.G. & Russo, A.L. 1967 "Recent Studies of Nonequilibrium Flows at the Cornell Aeronautical Laboratory". AGARD C.P. No. 12, p.443.

Hurle, I.R. 1971 "Nonequilibrium Flows with Special Reference to the Nozzle-Flow Problem". 8th Int. Shock Tube Symposium, London. Chapman & Hall.

Lapworth, K.C. & Townsend, J.E.G. 1967 "Temperature and Pressure Studies in the Reservoir of a Reflected Shock Hypersonic Tunnel". A.R.C. R. & M. 3479.

Lewis, M.J. & Bernstein, L. 1972 "Measurements of Temperature and Pressure behind the Incident and Reflected Shocks in a Shock Tube". A.R.C. C.P. No. 1239.

Russo, A.L.	1966	"Importance of Impurities on Vibrational Relaxation Measurements in N_2". J. Chem. Phys. 44 p.1305.
Russo, A.L. & Watt, W.S.	1968	"Infrared Measurements of the Vibrational Excitation and De-Excitation Rates of N_2 using CO Additive". Cornell Aero. Lab. Rep. AF-2567 - A - 1.
Wilson, J.L., Schofield, D. & Lapworth, K.C.	1967	"A Computer Program for Non-equilibrium Convergent-Divergent Nozzle Flows". N.P.L. Aero. Rep. 1250. A.R.C. 29 246.

Produced in England by Her Majesty's Stationery Office, Reprographic Centre, Basildon

R 74518/1/505376 K4 5 '74 TP

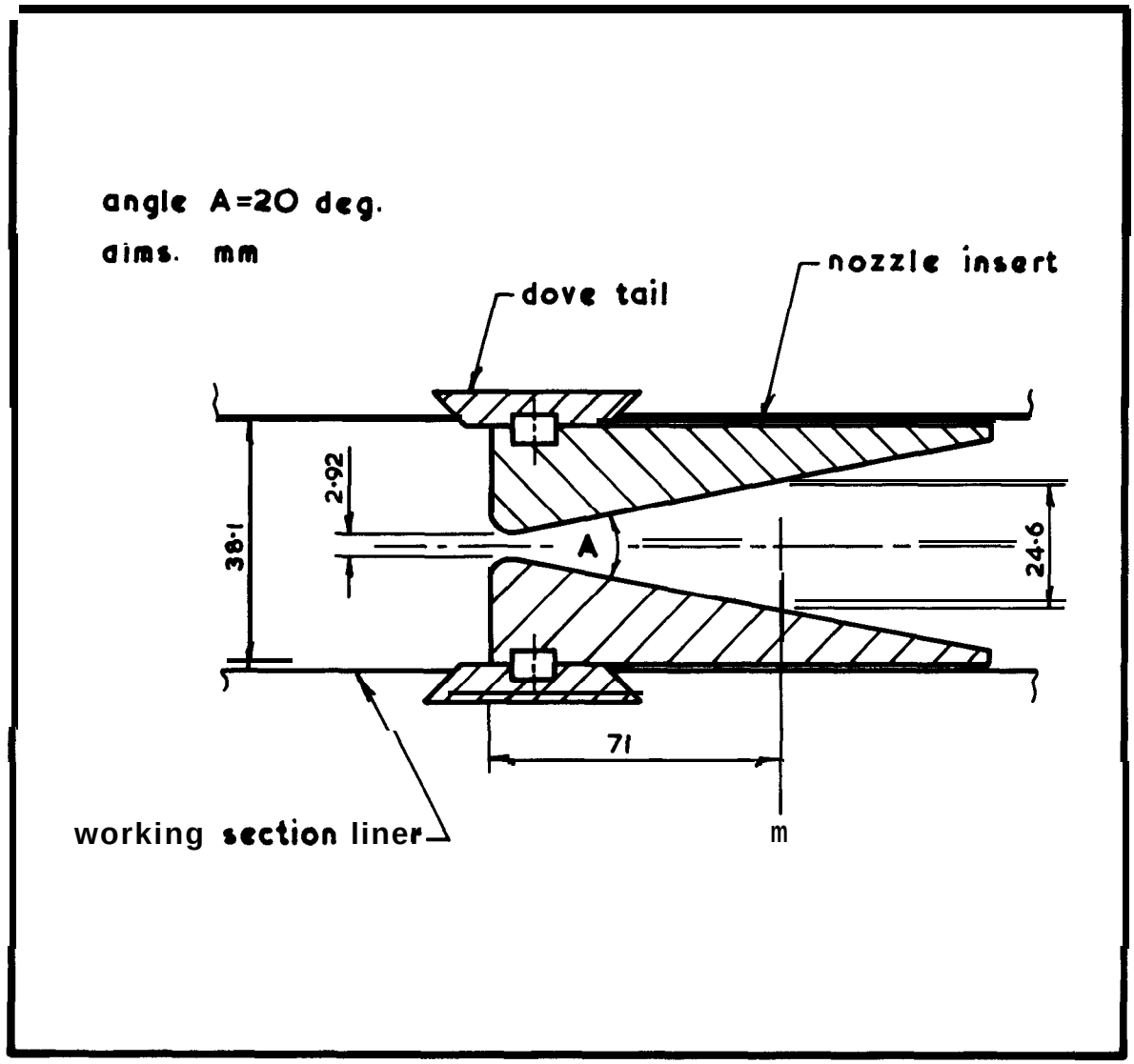

figure 1. The two-dimensional nor z le

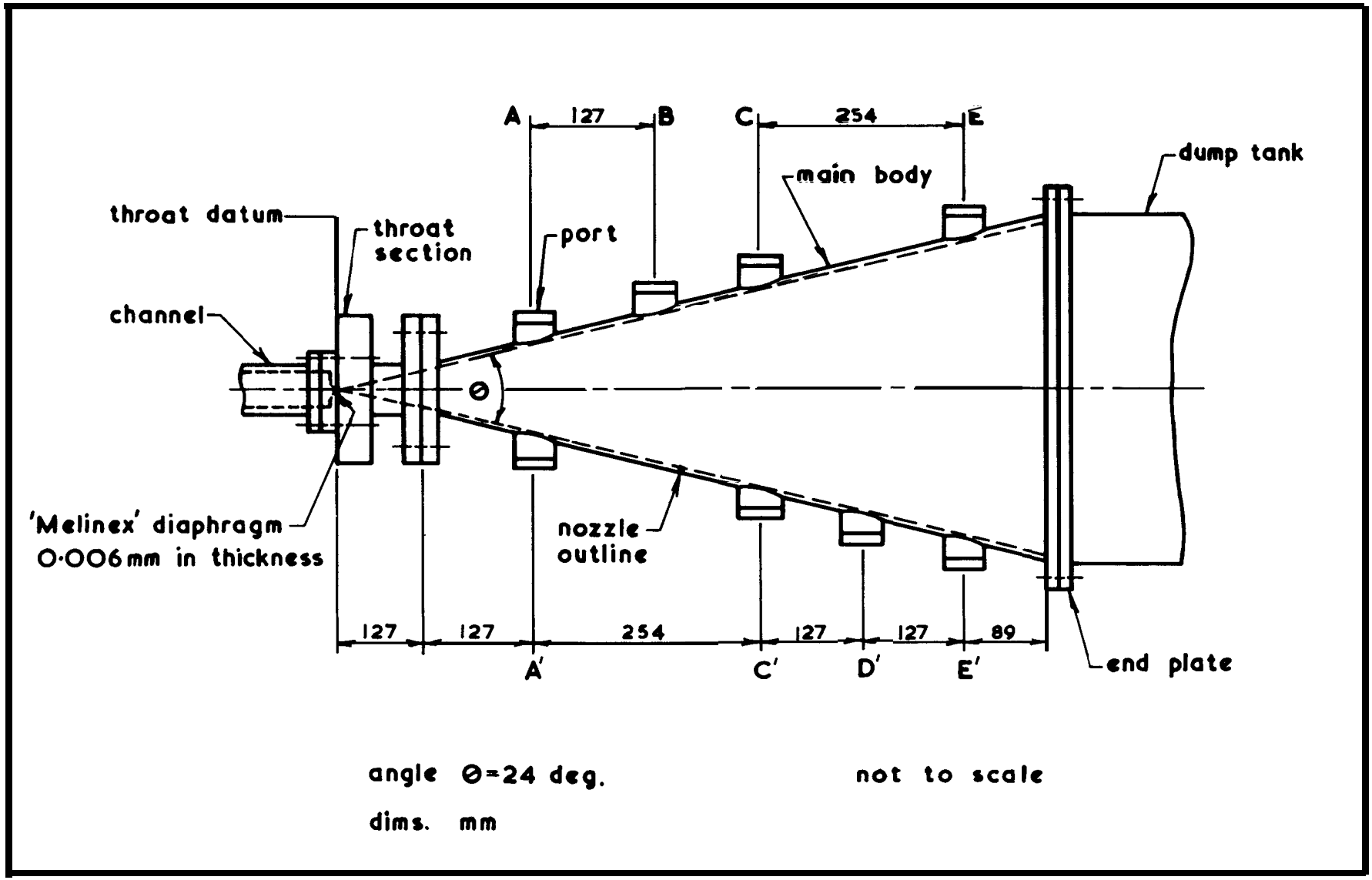

Figure 2 The conical nozzle

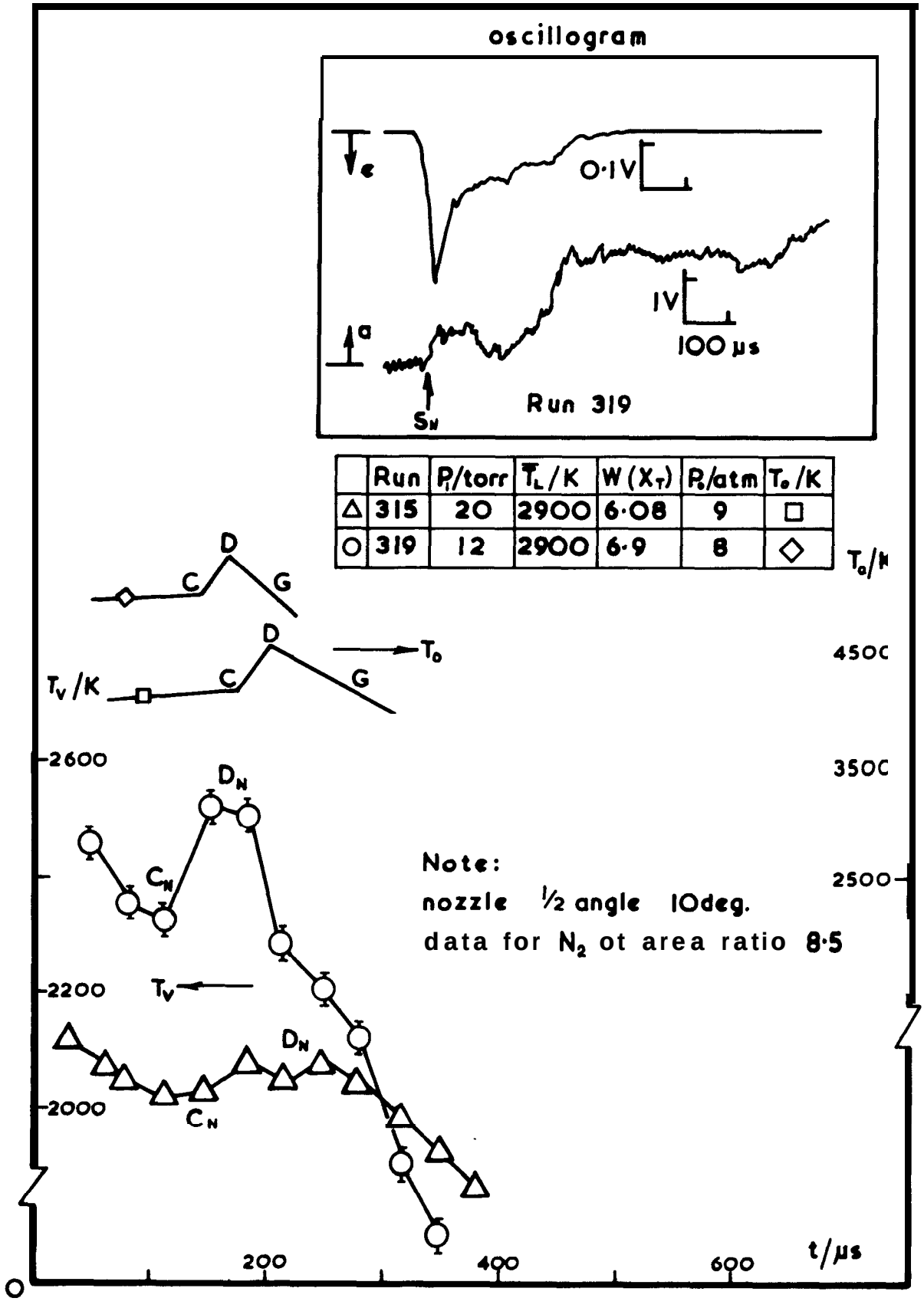

Figure 3 Vibrational temperature variation in 2D nozzle

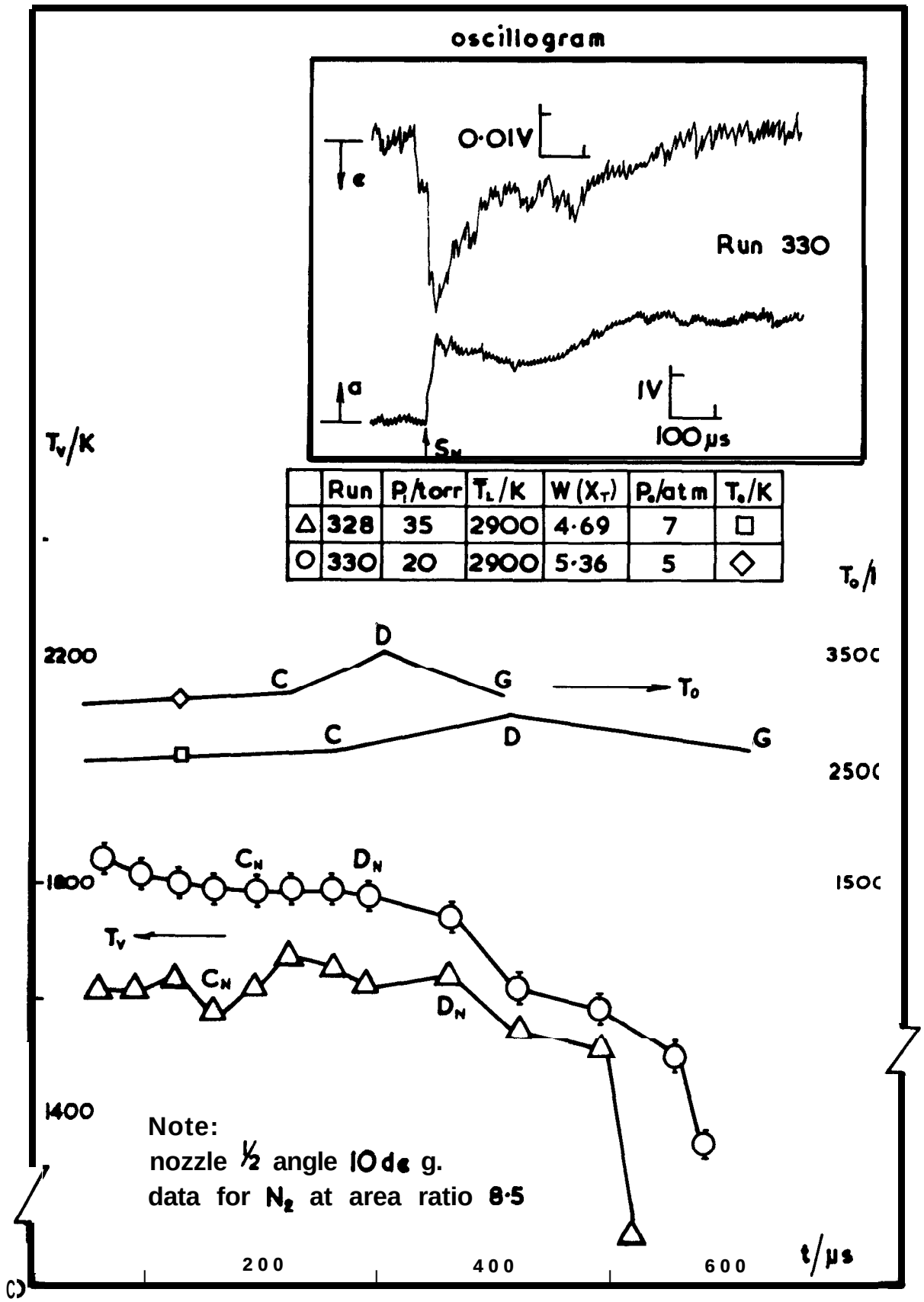

	Run	P_i/torr	T_L/K	W (X_T)	P_0/atm	T_0/K
△	328	35	2900	4·69	7	□
○	330	20	2900	5·36	5	◇

Figure 4 Vibrational temperature variation in 2D nozzle

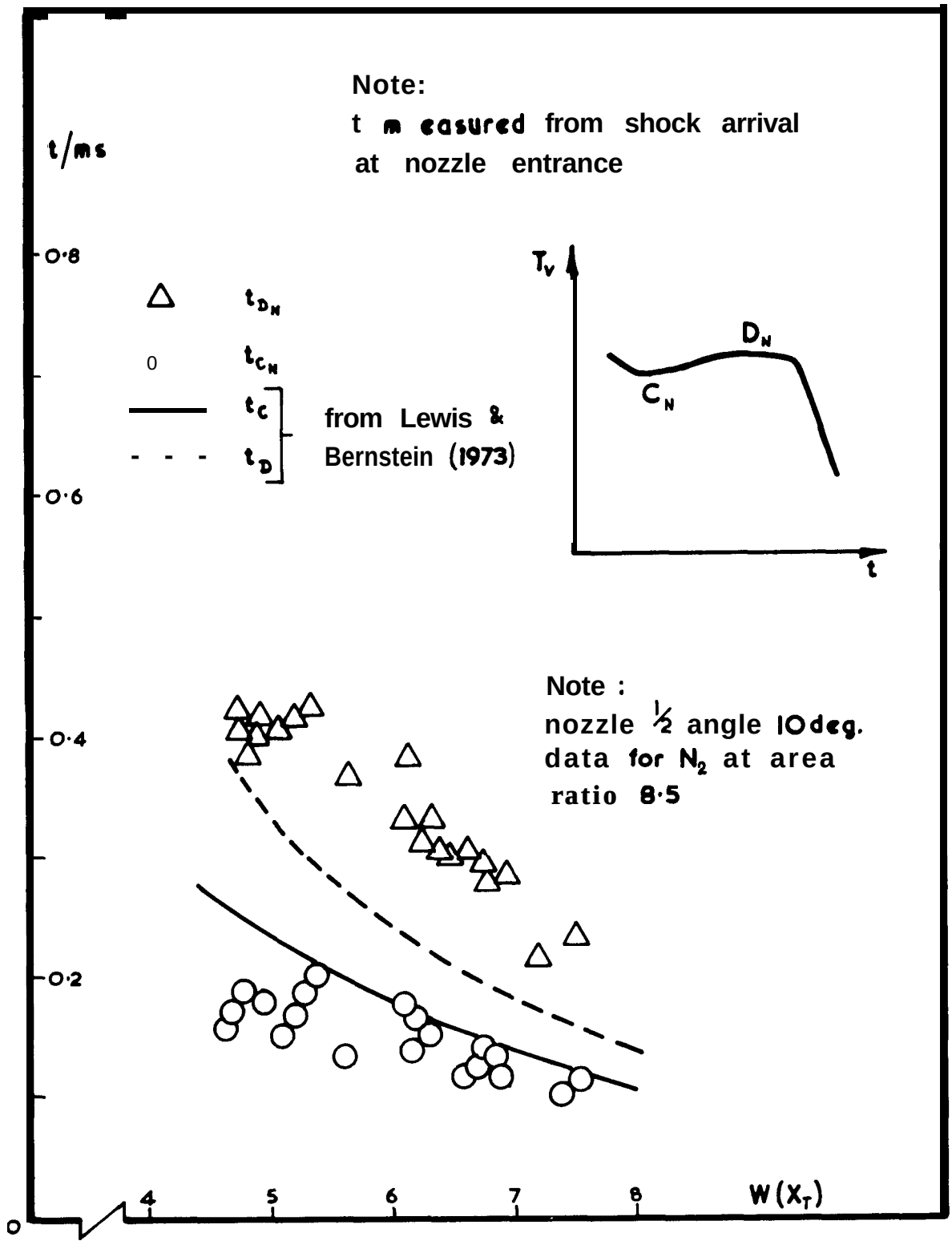

Figure 5 High temperature duration in 2D nozzle

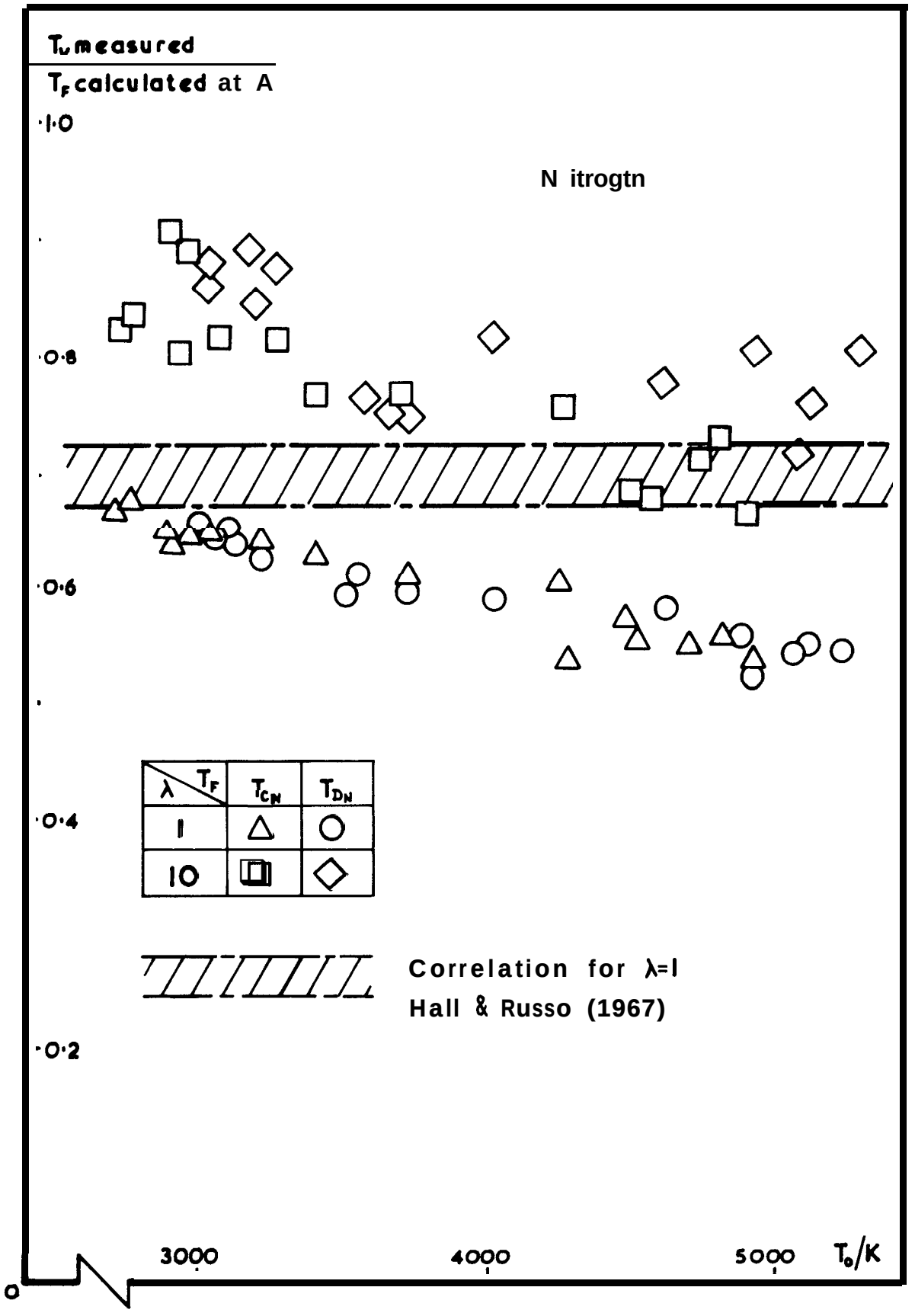

Figure 6 Measured vibrational temperatures compared with calculated f roze n temperatures for two-dimensiona l nozzle

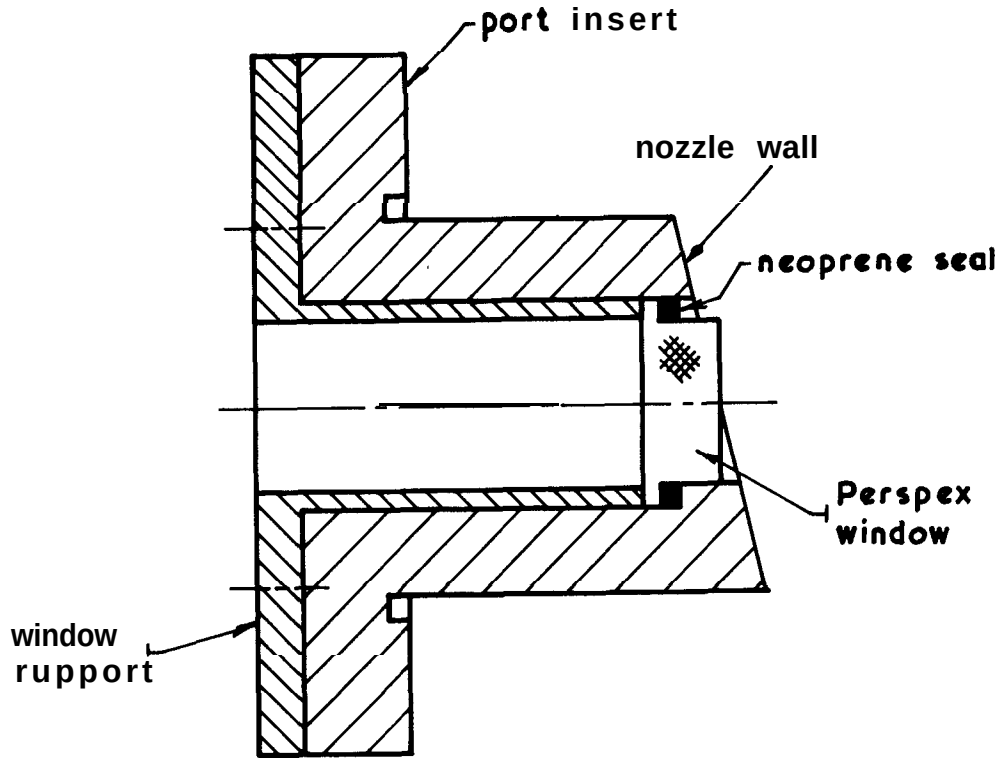

a. FLUSH MOUNTED WINDOWS

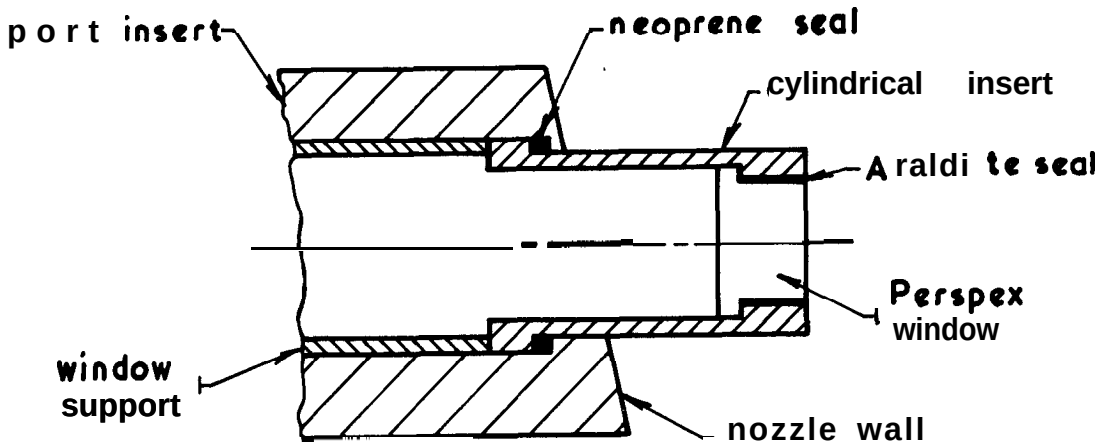

b. WINDOW EXTENSION

Scale 1:1

Figure 7 Conical nozzle window mountings

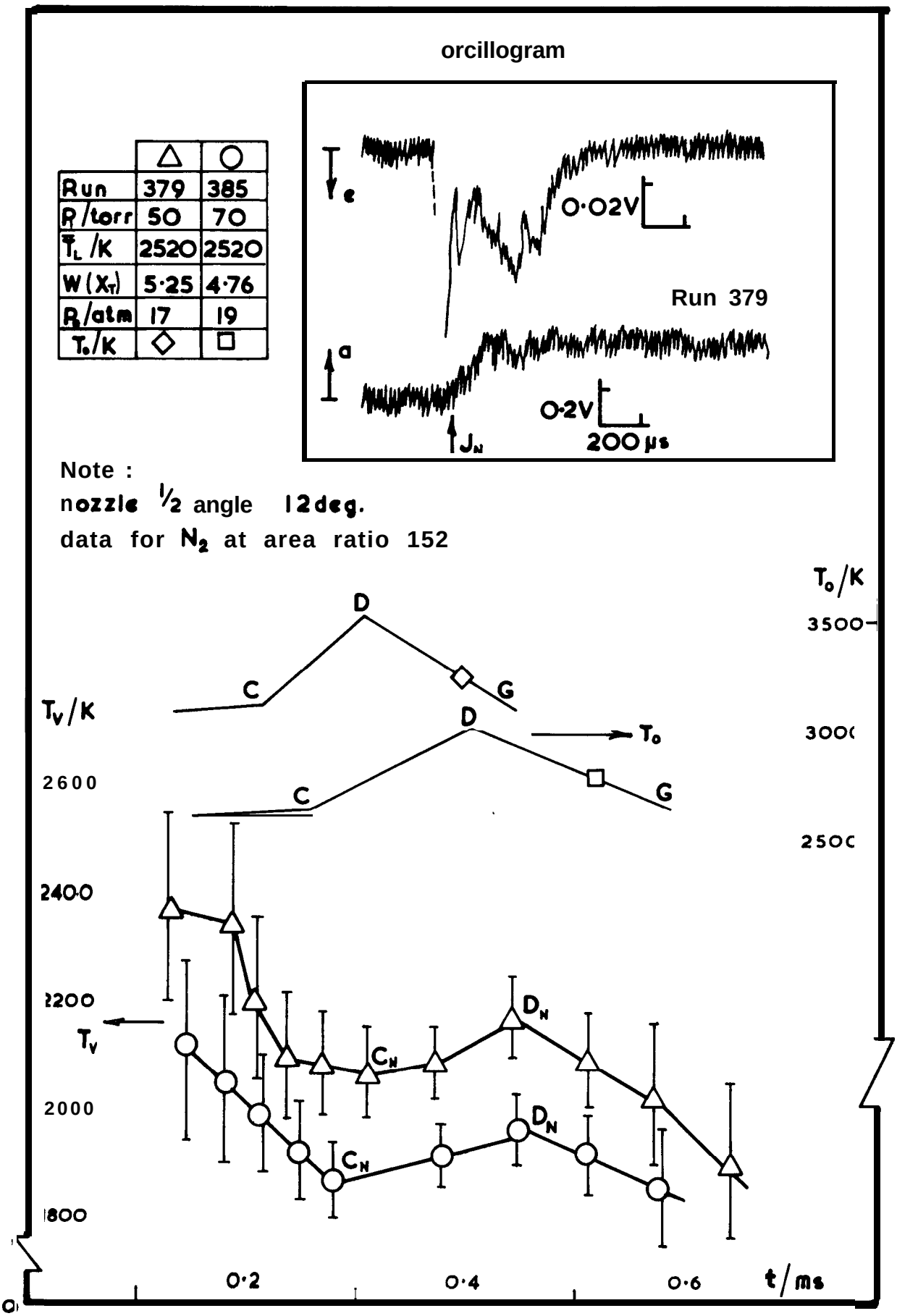

Figure 8 Vibrational temperature variation (conical nozzle)

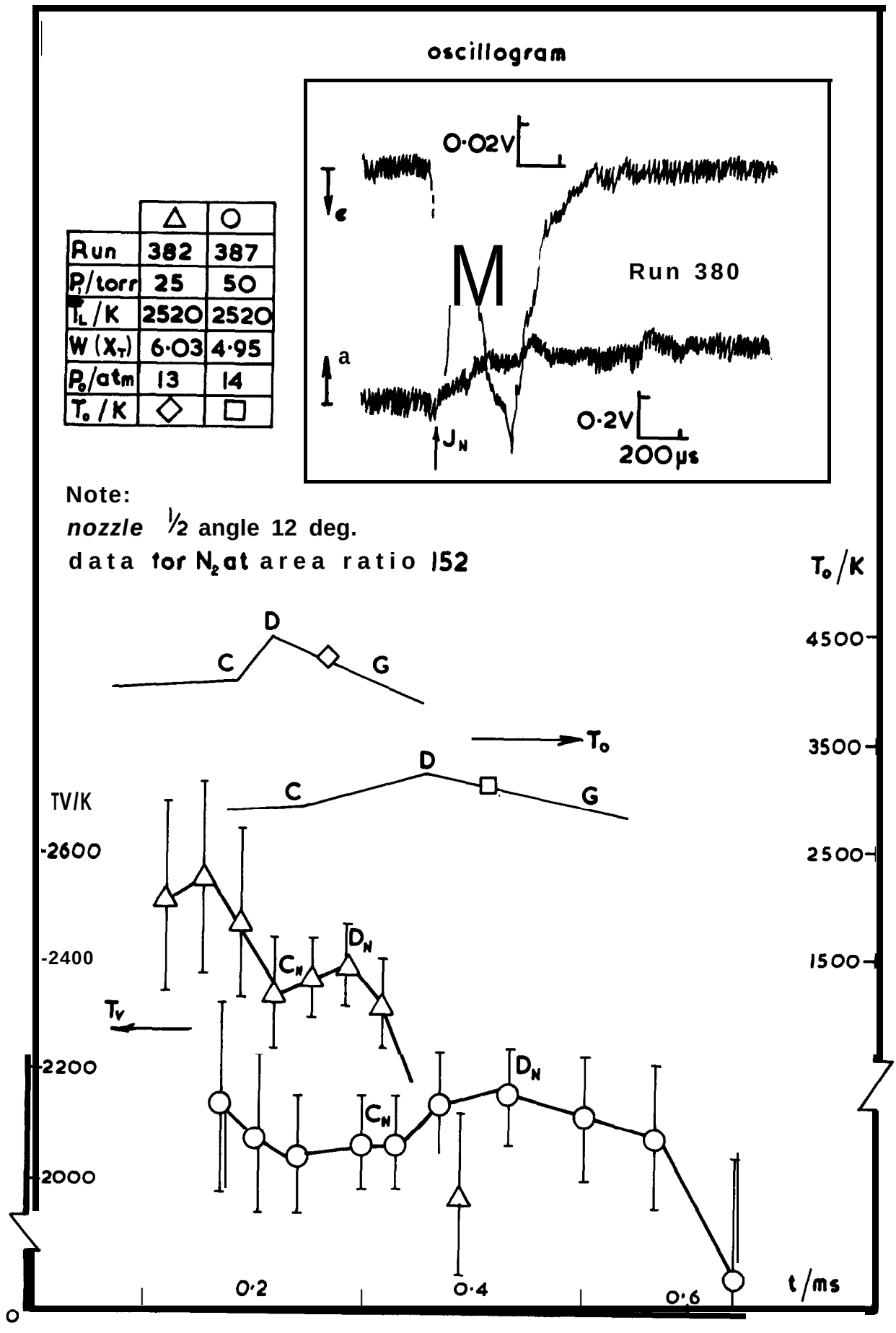

Figure 9 Vibrational temperature variation (conical nozzle)

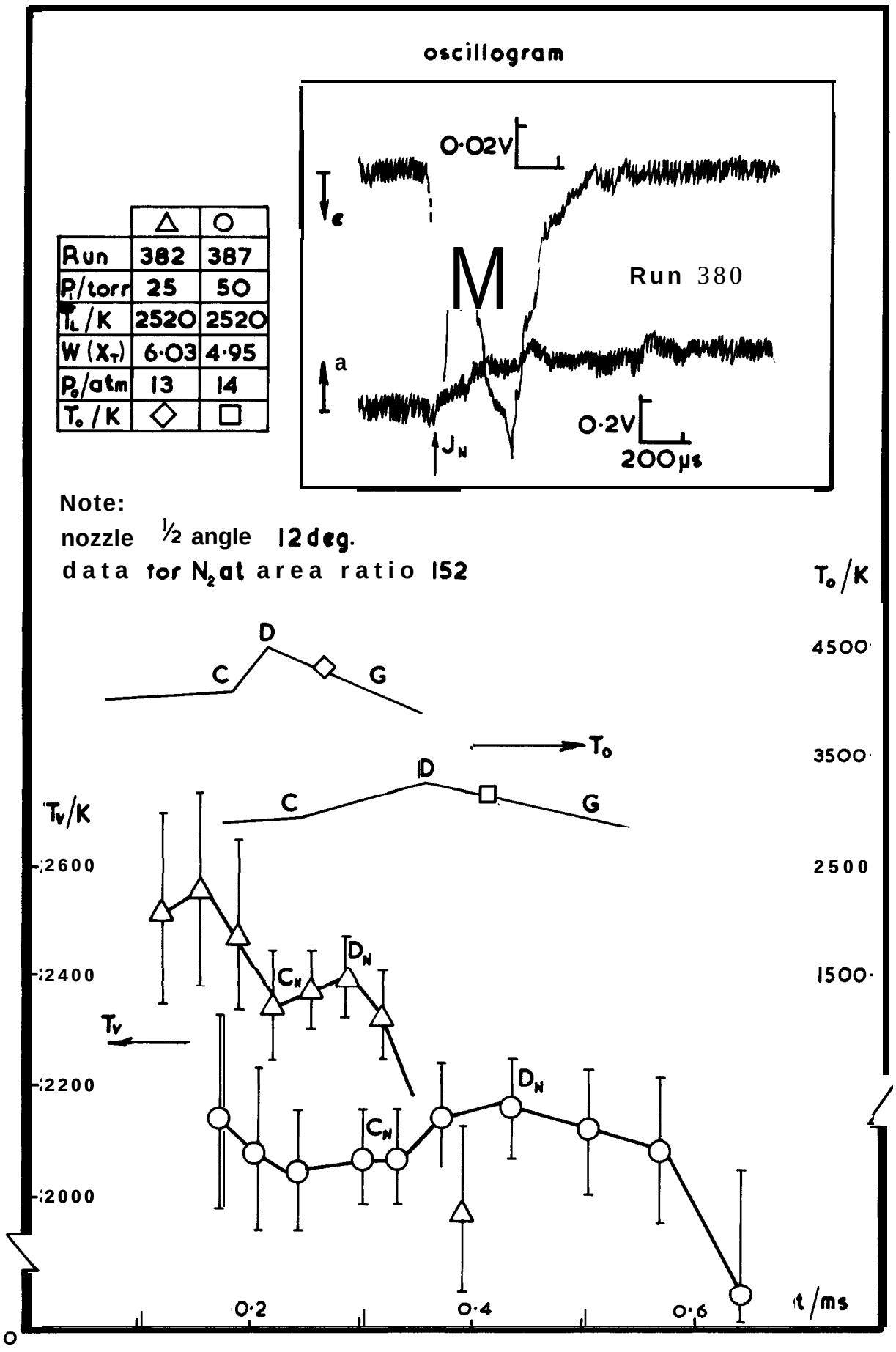

Figure 9 Vibrational temperature variation (conical nozzle)

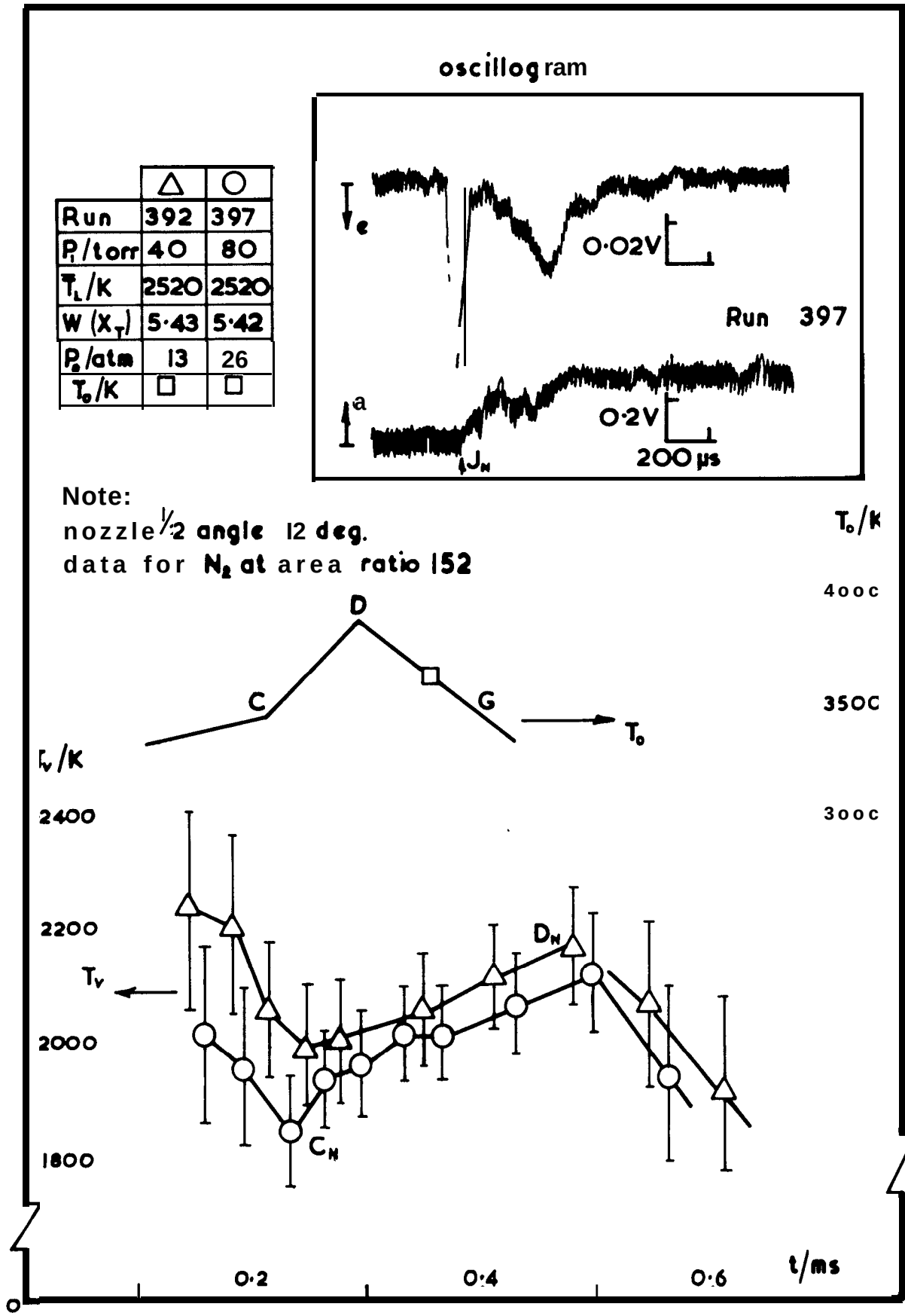

Figure 10 Vibrational temperature variation (conical nozzle)
identical stagnation temperature

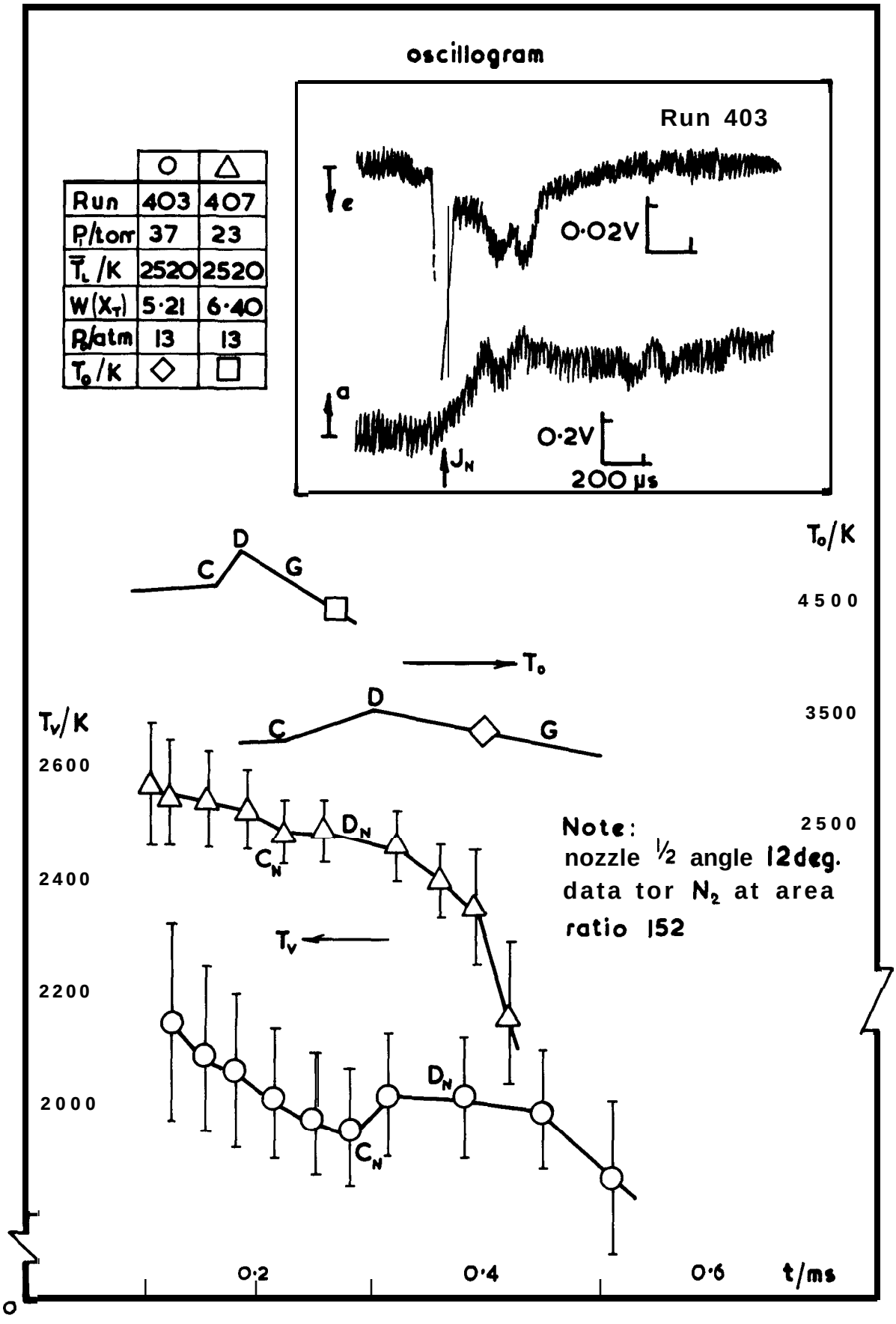

Figure II Vibrational temperature variation (conical nozzle) identical stagnation pressure

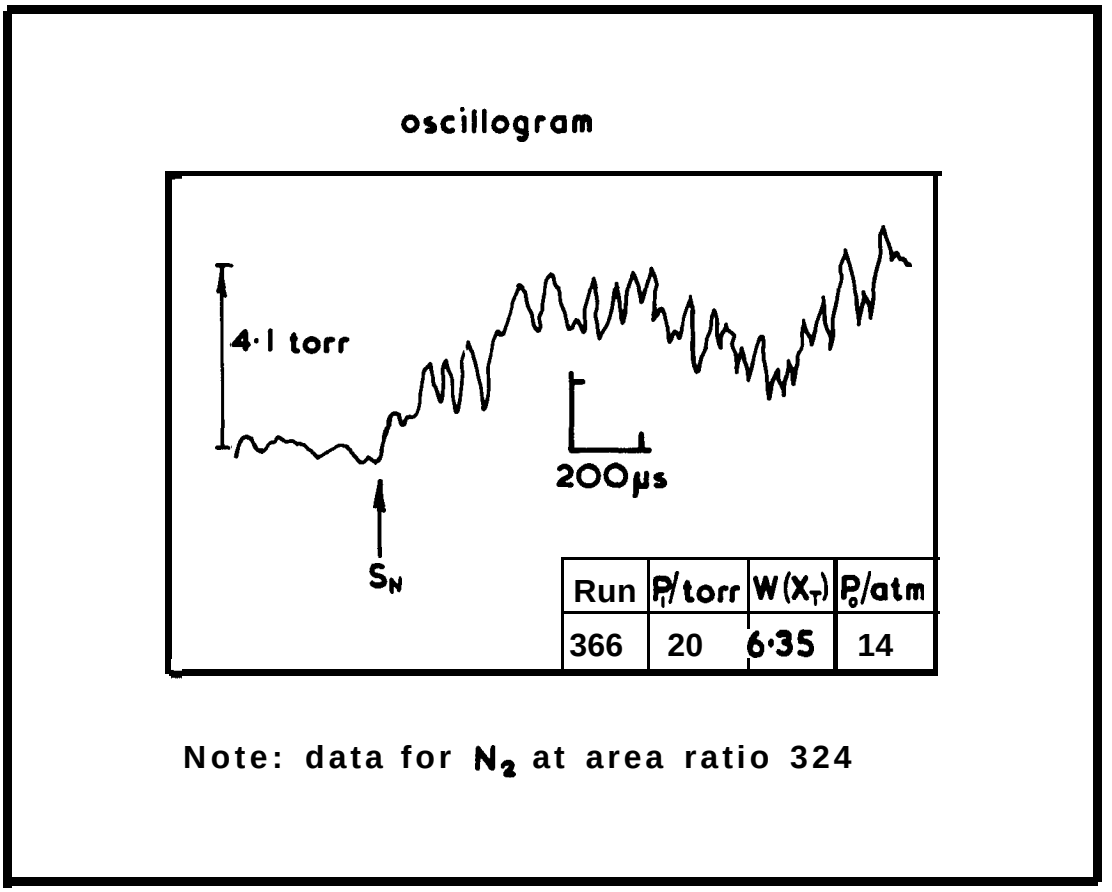

Figure 12 Static pressure variation at station B in the conical nozzle

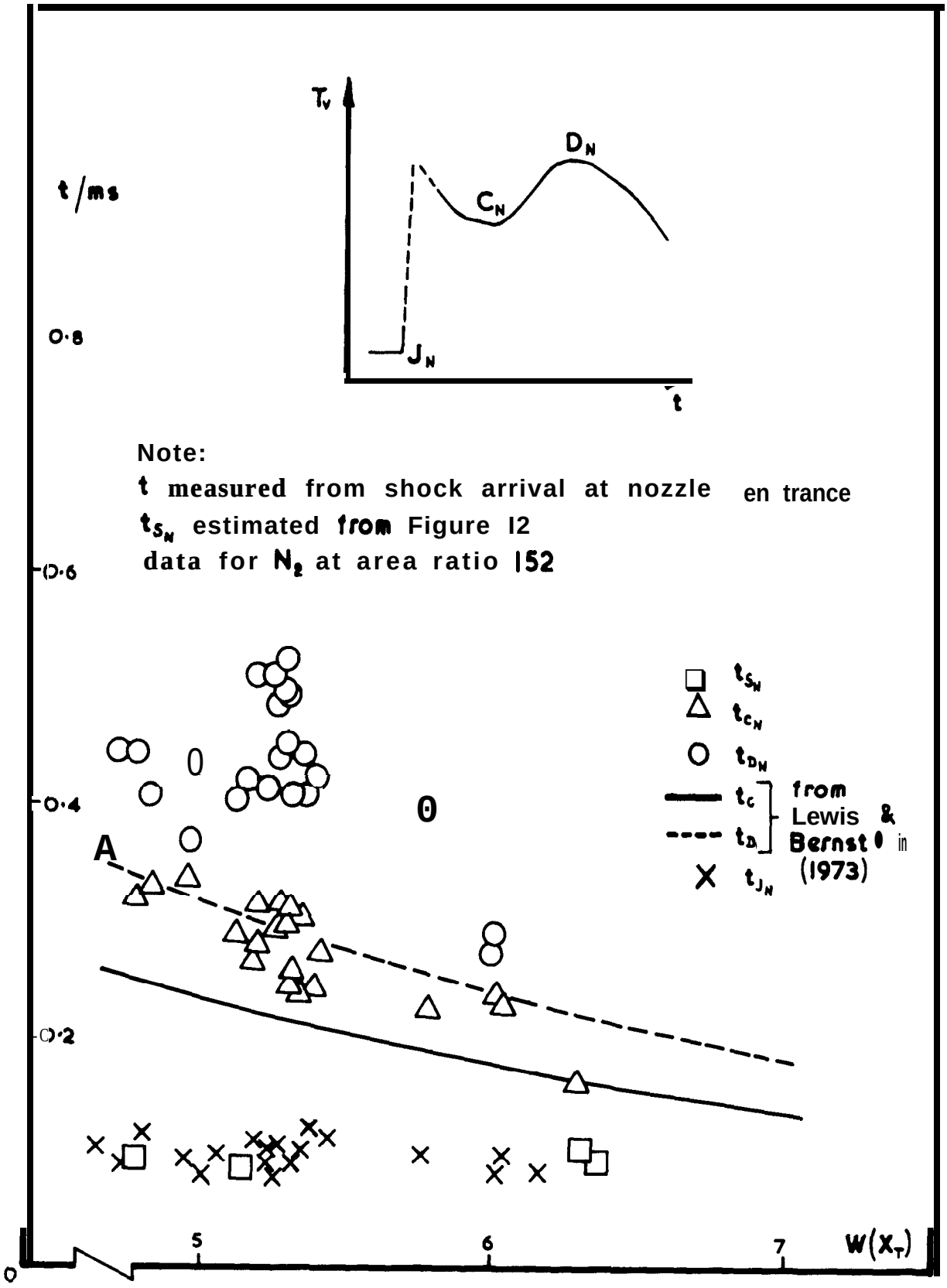

Figure 13 Hot flow duration at station AA' (conical nozzle)

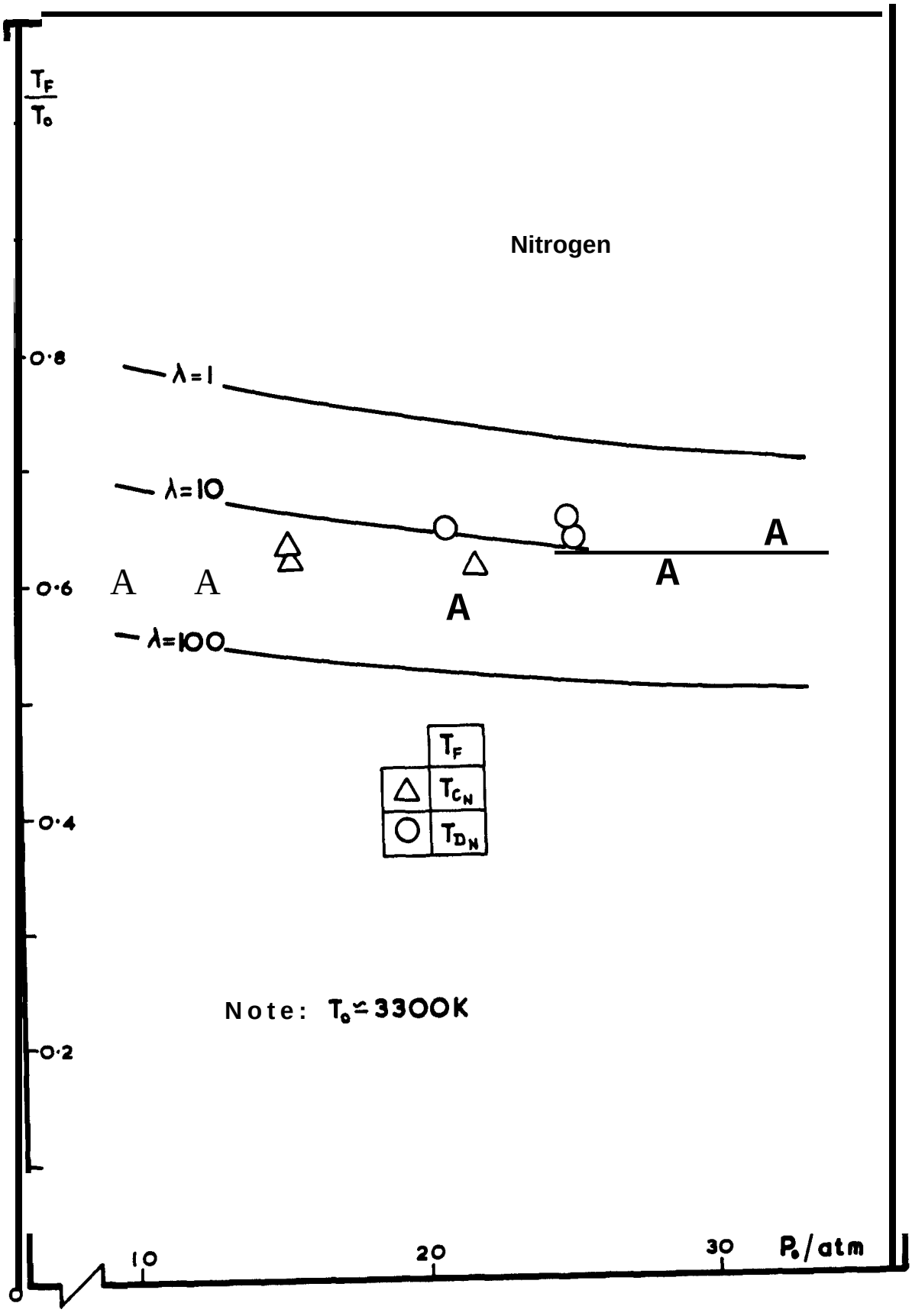

Figure 14 Calculated and measured frozen vibrational temperatures

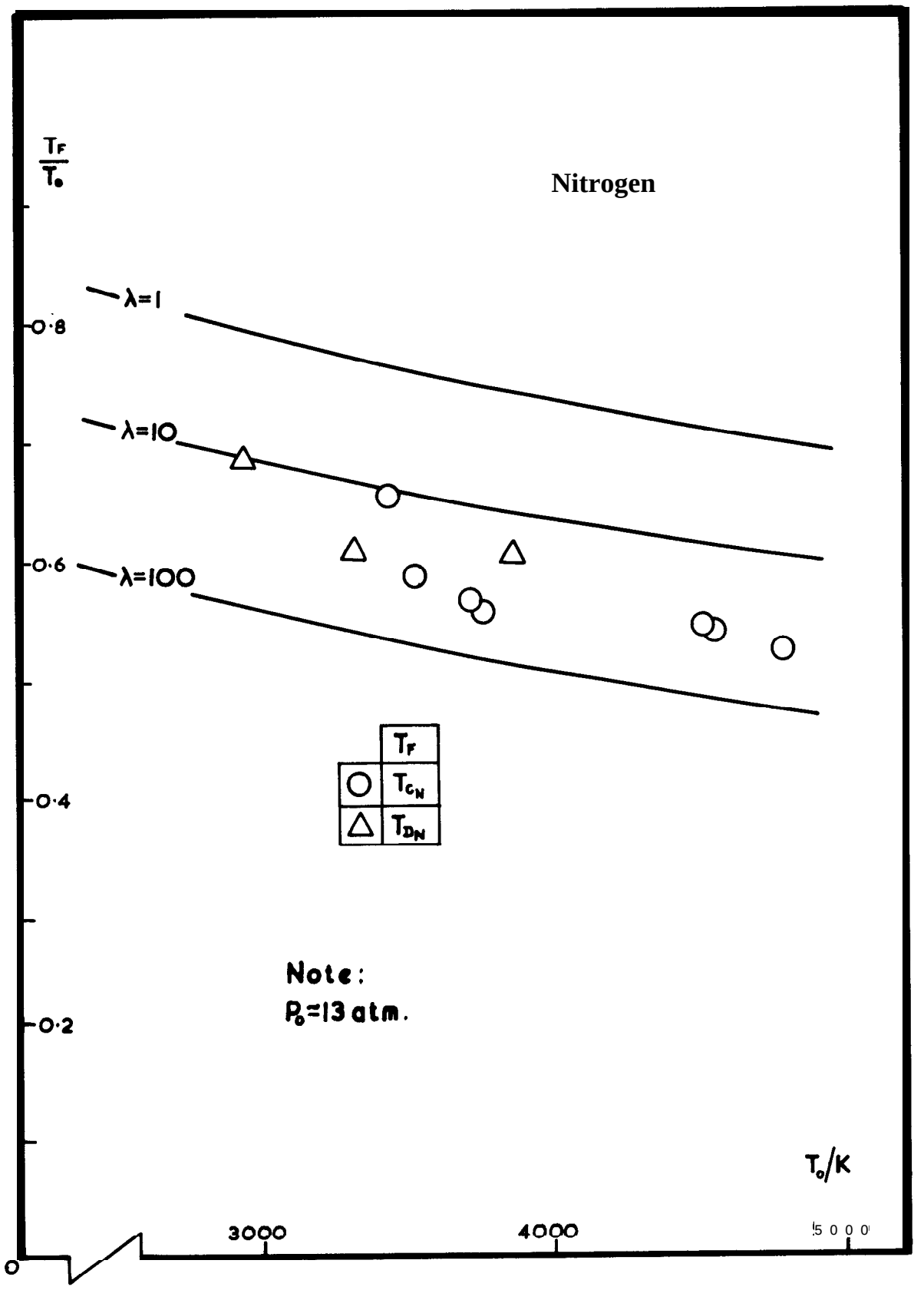

Figure 15 Calculated and measured frozen vibrational temperatures

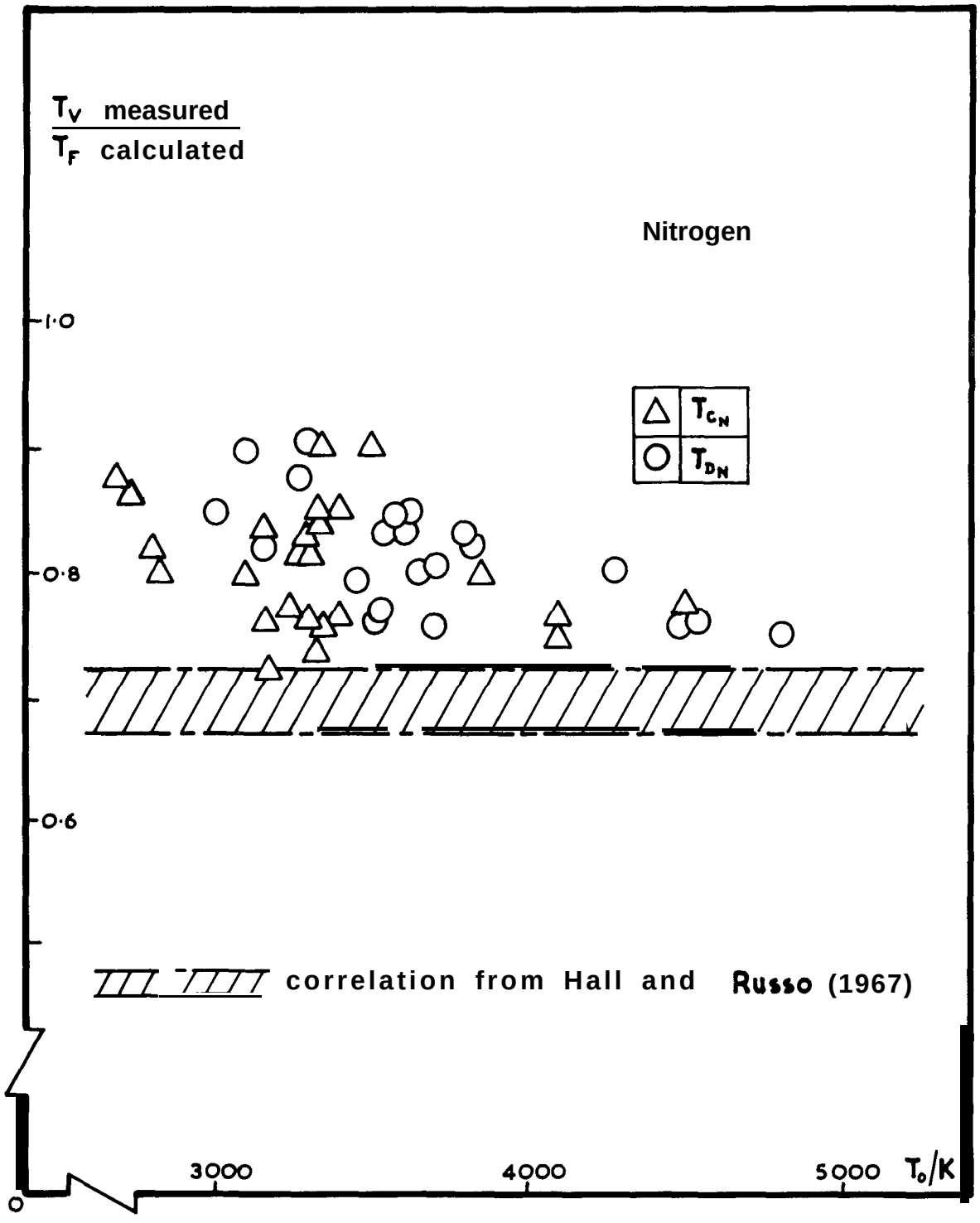

Figure 16 Correlation of frozen vibrational temperatures in the conical nozzle

HER MAJESTY'S STATIONERY OFFICE

Government Bookshops

49 Htgh Holborn, London WC1V 6HB
13a Castle Street, Edmburgh EH2 3AR
41 The Hayes, Cardiff CFMSW
Brazennose Street, Manchester M60 8AS
Southey House, Wine Street, Bristol BS1 2BQ
258 Broad Street, Birmingham B1 2HE
80 Chichester Street, Belfast BT1 4JY

Government publications are also available through booksellers

C.P. No. 1294

ISBN 011 470878 9